bioRxiv preprint doi: https://doi.org/10.1101/157362; this version posted June 29, 2017. The copyright holder for this preprint (which was not certified by peer review) is the author/funder, who has granted bioRxiv a license to display the preprint in perpetuity. It is made available under aCC-BY-NC-ND 4.0 International license.

Recapitulating bone development for tissue regeneration through engineered mesenchymal condensations and mechanical cues

Anna M. McDermott[1,2]*, Samuel Herberg[3]*, Devon E. Mason[1,2], Hope B. Pearson[2], James H. Dawahare[2], Joseph M. Collins[1,2,4], Mark W. Grinstaff[5], Daniel J. Kelly[6], Eben Alsberg[3,7,8†], Joel D. Boerckel[1,2,4†]

1. Department of Orthopaedic Surgery, Perelman School of Medicine, University of Pennsylvania, Philadelphia, PA.
2. Department of Aerospace and Mechanical Engineering, University of Notre Dame, Notre Dame, IN.
3. Department of Biomedical Engineering, Case Western Reserve University, Cleveland, OH.
4. Department of Bioengineering, University of Pennsylvania, Philadelphia, PA
5. Department of Mechanical Engineering, Trinity Center for Bioengineering, Trinity College Dublin, Dublin, Ireland.
6. Department of Biomedical Engineering, Boston University, Boston, MA
7. Department of Orthopaedic Surgery, Case Western Reserve University, Cleveland, OH.
8. National Center for Regenerative Medicine, Division of General Medical Sciences, Case Western Reserve University, Cleveland, OH.

* These authors contributed equally.
† Co-corresponding authors

Natural fracture healing recapitulates bone development through endochondral ossification,[1] resulting in clinical success rates of 90-95%.[2] However, large bone defects of critical size cannot form a callus and exhibit high rates of complication and non-union even after intervention.[3] Bone tissue engineering holds promise, but traditional approaches have focused on direct, intramembranous bone formation.[4] We propose that mimicking the endochondral process that is naturally selected for bone development and fracture repair may improve regenerative outcome. Since physical stimuli are critical for proper endochondral ossification during bone morphogenesis[5,6] and fracture healing,[7–9] mechanical loading may be essential to enable reliable endochondral defect regeneration as in callus-mediated fracture repair. Here we report that *in vivo* mechanical loading, via dynamically tuned fixator compliance, restored bone function through endochondral ossification of engineered human mesenchymal condensations. The condensations mimic limb bud morphogenesis in response to local morphogen presentation by incorporated gelatin microspheres. Endochondral regeneration in large defects exhibited zonal cartilage and woven bone mimetic of the native growth plate, with active YAP signaling in human

bioRxiv preprint doi: https://doi.org/10.1101/157362; this version posted June 29, 2017. The copyright holder for this preprint (which was not certified by peer review) is the author/funder, who has granted bioRxiv a license to display the preprint in perpetuity. It is made available under aCC-BY-NC-ND 4.0 International license.

hypertrophic chondrocytes *in vivo.* Mechanical loading regulated vascular invasion and enhanced endochondral regeneration, with an order-of-magnitude greater response to loading than that observed for intramembranous repair,[10–12] restoring intact bone properties. This study represents the first demonstration of the effects of mechanical loading on transplanted cell-mediated bone defect regeneration and establishes the importance of *in vivo* mechanical cues, cellular self-organization, and inductive signal presentation for recapitulation of development for tissue engineering.

Long bone morphogenesis is initiated by condensation of mesenchymal cells in the early limb bud, which differentiate and mature into the cartilaginous anlage that gives rise to endochondral bone formation. This process is dependent on both local morphogen gradients and mechanical forces *in utero*.[6,13] Natural bone fracture healing recapitulates endochondral bone development, but only under conditions of compressive interfragmentary strain.[14,15] Without mechanical loading, fractures will heal through direct, intramembranous bone formation,[9] implicating mechanical cues as essential regulators of endochondral ossification. The emerging paradigm of biomimetic tissue engineering approaches aim to replicate this process,[16,17] but functional endochondral bone regeneration using transplanted human progenitor cells remains elusive potentially due to insufficient recapitulation of the essential cellular, biochemical, and mechanical stimuli. We engineered scaffold-free human mesenchymal stem cell (hMSC) condensations through cellular self-assembly into sheets.[18] By incorporating morphogen-releasing gelatin microspheres into the condensations, TGF-β1 was spatially distributed throughout the condensations and released with the aim of driving endochondral lineage progression upon implantation. We controlled *in vivo* mechanical loading through dynamic modulation of fixation plate compliance.[10,19]

Engineered mesenchymal condensations, self-assembled into sheets of 2 x 10^6 cells and 600 ng TGF-β1, exhibited homogeneous cellular organization without histologically detectable sulfated glycosaminoglycan (sGAG) deposition or bone formation at the time of implantation (i.e., two days *in*

bioRxiv preprint doi: https://doi.org/10.1101/157362; this version posted June 29, 2017. The copyright holder for this preprint (which was not certified by peer review) is the author/funder, who has granted bioRxiv a license to display the preprint in perpetuity. It is made available under aCC-BY-NC-ND 4.0 International license.

vitro culture) (Fig. 1a, Extended Data Fig. 1a). Cellular organization was qualitatively similar to that of the developing mouse limb bud at E11.5-12.5 (Fig. 1b, Extended Data Fig. 1b). Local TGF-β1 presentation upregulated and sustained mRNA expression of Sox9, Aggrecan, and Collagen 2a1 (Fig. 1c), indicating chondrogenic lineage priming, with limited expression of osteogenic markers, further mimicking the gene expression patterns exhibited in the mouse limb bud at E11.5-12.5 (cf. refs. [20,21]). After 21 days of further *in vitro* culture, local TGF-β1-treated condensations exhibited characteristically-shaped chondrocytes and substantial sGAG matrix (Fig. 1d), demonstrating chondrogenic differentiation without additional growth factor supplementation in the media.

While the molecular mechanisms that control endochondral ossification remain incompletely understood, recent evidence from our lab and others implicates the mechanosensitive transcription factor[22] Yes-associated protein (YAP) as a mechanosensitive,[22] TGF-β1-inducible[23] regulator of progenitor cell lineage specification, promoting endochondral bone development[24] but inhibiting chondrogenesis.[25] Consistent with these reports, we observe that TGF-β1 presentation transiently upregulated transcription of the angiogenic YAP target gene Cyr61 (Fig. 1c) and increased YAP protein levels (Fig. 1e, top row), while Cyr61 expression was reduced in differentiated chondrocytes at day 23 (Fig 1e, bottom row), consistent with an inhibitory role of YAP in embryonic limb bud chondrogenesis.[25] Together, these data demonstrate our capacity to recapitulate the early limb bud in engineered mesenchymal condensations and suggest that YAP may play a role in mechanical regulation of endochondral lineage progression during regeneration.

bioRxiv preprint doi: https://doi.org/10.1101/157362; this version posted June 29, 2017. The copyright holder for this preprint (which was not certified by peer review) is the author/funder, who has granted bioRxiv a license to display the preprint in perpetuity. It is made available under aCC-BY-NC-ND 4.0 International license.

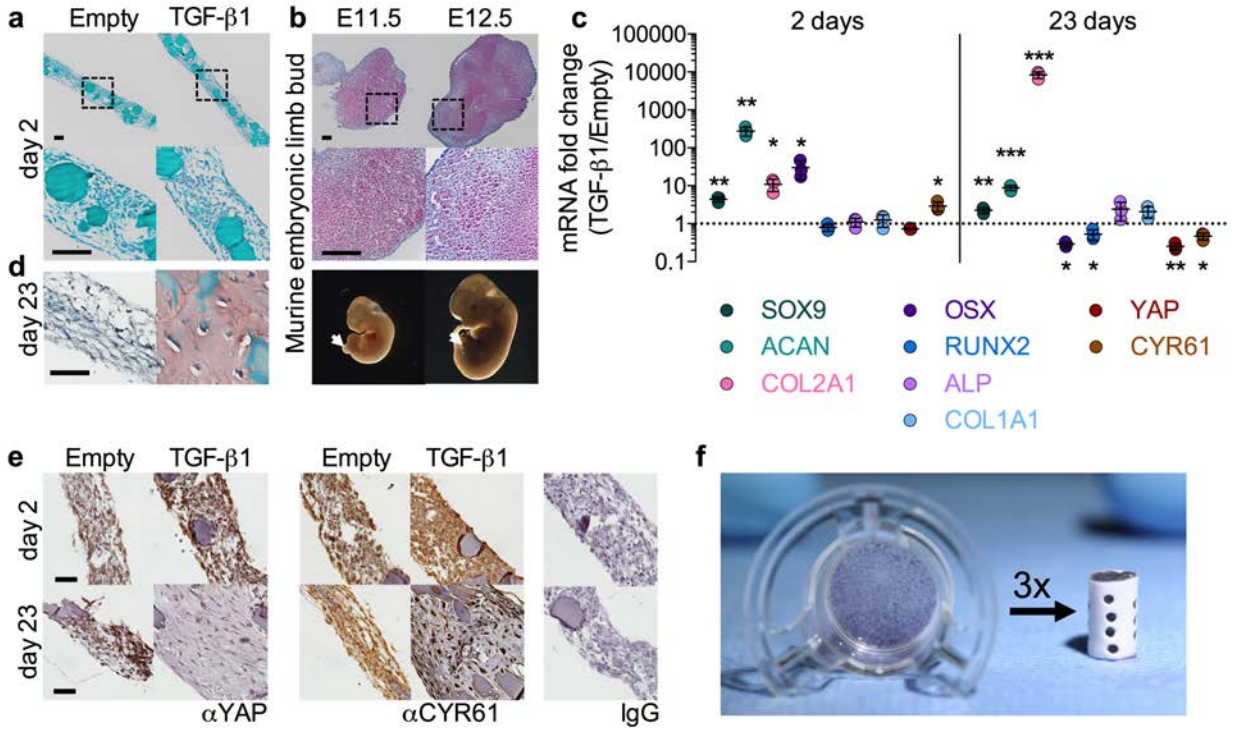

Figure 1: Engineered mesenchymal condensations mimic the embryonic limb bud. a, Safranin-O/Fast green staining of hMSC sheets with empty gelatin microspheres (left), or loaded with 600 ng TGF-β1 (right) cultured for two days on transwell inserts. Bottom: magnification of enclosed areas. **b**, Safranin-O/Fast green staining of murine limb buds at embryonic days 11.5 and 12.5 (E11.5, E12.5). Bottom: photomicrographs of embryos with limb buds indicated by arrows. **c**, Messenger RNA expression of chondrogenic, osteogenic, and YAP pathway genes at day two *in vitro*; qRT-PCR results were normalized to GAPDH and expressed as fold-change over empty control sheets (n = 3 sheets per group). **d**, Safranin-O/Fast green staining of sheets at day 23 *in vitro*. **e**, Immunostaining for YAP and target gene CYR61 at days 2 and 23 *in vitro*. Right: negative control isotype IgG (rabbit, top; mouse, bottom). **f** Photograph of hMSC sheet cultured 2 days on transwell insert (left) and engineered mesenchymal condensation for implantation (right), assembled from three sheets within a perforated electrospun mesh tube. *p<0.05, **p<0.01, ***p<0.001 TGF-β1 treated vs. empty, unpaired two-tailed Student's t-test for each independent gene, with corrections for multiple comparisons by the Bonferroni method. Data shown with mean ± s.d. Scale bars, 100 μm. Histological images are representative of three independent samples per group.

bioRxiv preprint doi: https://doi.org/10.1101/157362; this version posted June 29, 2017. The copyright holder for this preprint (which was not certified by peer review) is the author/funder, who has granted bioRxiv a license to display the preprint in perpetuity. It is made available under aCC-BY-NC-ND 4.0 International license.

To evaluate the capacity of engineered mesenchymal condensations to induce endochondral bone regeneration, we created cylindrical condensations (8 mm length, 5 mm diameter) for *in vivo* implantation. These were compiled by placing three hMSC sheets (after 2 days maturation *in vitro*) into perforated electrospun polycaprolactone nanofiber mesh tubes[26] (Figure 1f), for a total of $6x10^6$ cells and 1.8 μg of TGF-β1 per construct. Condensations were then implanted in critical-sized (8 mm) bone defects, surgically created in femora of athymic Rowett nude rats (RNU), as described previously.[10,27]

Proper endochondral ossification in both bone development and fracture healing requires mechanical stimuli,[5,6,28] but the effects of *in vivo* mechanical loading on endochondral bone defect regeneration are incompletely understood, and the effects in vivo loading transplanted cell-mediated repair has not been studied. Here, we controlled ambulatory load transfer *in vivo* using custom internal fixation plates capable of temporal control of axial stiffness by elective unlocking.[10,11,19] The timing and magnitude of mechanical forces imparted to the defects were controlled in three groups: stiff (control, n = 11), early (immediate loading, n = 9), and delayed (plates unlocked to initiate loading at week 4, n = 9) (Extended Data Video 1). The multi-modal mechanical behavior of the plates was assessed by *ex vivo* mechanical testing (stiff: k_{axial} = 260 ± 28 N/mm, locked compliant: k_{axial} = 250 ± 35 N/mm, unlocked compliant: k_{axial} = 8.0 ± 3.5 N/mm; mean ± s.d.; Extended Data Figure 2). Approximations based on published femoral loading during the rat gait cycle[29] and rule-of-mixtures theory from linear elasticity to quantify load-sharing between the fixation plates and the defect indicate that interfragmentary strains at day 0 reach 2-3% in the stiff and delayed groups, and up to 10-15% in the early group. A recent *in vivo* strain sensor study using a modified version of the stiff plates described here confirmed these numbers within one percent for the stiff group.[30] The amount of strain experienced over time is a function of the load sharing, and therefore dependent on the amount, type, and kinetics of tissue ingrowth; however, using data from the studies below, we estimate strains of 5-10% upon plate unlocking at week 4 in the delayed group, with all groups converging on 0.5-3% by week 12.

bioRxiv preprint doi: https://doi.org/10.1101/157362; this version posted June 29, 2017. The copyright holder for this preprint (which was not certified by peer review) is the author/funder, who has granted bioRxiv a license to display the preprint in perpetuity. It is made available under aCC-BY-NC-ND 4.0 International license.

Bone regeneration progressed through endochondral ossification, exhibiting zonal cartilage and woven bone mimetic of the native growth plate by week 4 (Fig. 2a,b), similar to fracture callus recapitulation of development.[1] Both early and delayed loading significantly enhanced bone formation (Fig. 2, Extended Data Figs. 3, 4, 5, Video 1) as measured by bone volume (Fig. 2c) and bone volume fraction (Extended Data Fig. 3a). Notably, loading elevated bone accumulation rate between weeks 4 and 8 (cf. slopes of bone volume vs. time curves in Fig. 2c, quantification in Extended Data Fig. 3b). This coincided with load initiation in the early group and the stage of chondrocyte hypertrophy and transition to bone formation in all three groups (Fig. 3b, Extended Data Fig. 4). These findings are consistent with developmental studies showing that inhibition of fetal muscle contraction impairs endochondral ossification through reduced chondrocyte hypertrophy and ossification[5,6], a deficiency that can be rescued by dynamic loading *ex vivo*.[31] Though early loading significantly enhanced bone formation (Fig. 2c), the bone volume response in this group was variable (Extended Data Fig. 3a,c) and exhibited a significantly lower bridging rate compared to delayed loading (2/8 vs. 6/8, $p<0.05$ Chi square test, Extended Data Fig. 3d,e) due to persistent regions of non-mineralized cartilage and fibrocartilage (Fig. 3a, Extended Data Fig. 4), similar to the pseudarthroses induced by large-deformation cyclic bending.[32] In contrast, delayed loading induced robust bone formation with consistent bridging rate (Fig. 2c, Extended Data Fig. 3c,d).

Subsequently, we evaluated bone regeneration by the current clinically-used approach, "Infuse"[33] (shown in gray in Fig. 2c). This group featured 5μg rhBMP-2 delivery on absorbable collagen sponge as described previously[4]. While comparisons with the endochondral groups were not evaluated statistically, as these samples were performed in a separate surgery, endochondral repair was qualitatively slower during the first four weeks, consistent with progression through endochondral ossification, but was equivalent or qualitatively greater in the endochondral groups with early or delayed loading (Fig. 2c) suggesting bone regeneration at least equivalent to high-dose BMP-2 delivery.

bioRxiv preprint doi: https://doi.org/10.1101/157362; this version posted June 29, 2017. The copyright holder for this preprint (which was not certified by peer review) is the author/funder, who has granted bioRxiv a license to display the preprint in perpetuity. It is made available under aCC-BY-NC-ND 4.0 International license.

Notably, the mechanoresponse observed for endochondral regeneration (181% increase in bone volume compared to control) was an order-of-magnitude greater than that found previously for BMP-2-induced repair dominated by intramembranous ossification (18-20% increase) as observed both by our group[10,11] and others.[12] Quantitative densitometry (Fig. 2d, Extended Data Fig. 5d) and region of interest analyses (Extended Data Fig. 5a,b) revealed mineral concentration at the defect periphery, indicative of a cortical shell in all three groups. The bone formed within this cortex exhibited well-defined trabecular architecture similar to native femoral head trabecular bone as assessed by both microCT morphometry (Fig. 2e,g, Extended Data Fig. 5c-f) and histology (Fig. 2f, Extended Data Fig. 4, 6).

In cell-based tissue engineering strategies it is essential to understand the functional role of the transplanted cells. When driven down the endochondral pathway, viable donor cells have been observed up to several weeks after implantation,[34,35] in contrast to intramembranous-based approaches, which commonly exhibit rapid cell death due to lack of vascular and nutrient supply.[27] Further, recent reports suggest that hypertrophic chondrocytes may also transdifferentiate into bone-forming cells.[36–38] Therefore, to first test whether the transplanted cells functionally contributed to bone repair, we prepared identical mesenchymal condensations ($6x10^6$ cells and 1.8 μg of TGF-β1 per construct) for implantation after devitalization by freeze-thaw cycling. These displayed qualitatively reduced bone formation compared to live stiff plate controls (Fig. 2c,h, Extended Data Video 1) with fibrotic tissue filling the defect (Fig. 2i). Comparisons with the devitalized samples were not assessed statistically due to surgical operation at a separate time, but suggest a functional role of the transplanted cells.

bioRxiv preprint doi: https://doi.org/10.1101/157362; this version posted June 29, 2017. The copyright holder for this preprint (which was not certified by peer review) is the author/funder, who has granted bioRxiv a license to display the preprint in perpetuity. It is made available under aCC-BY-NC-ND 4.0 International license.

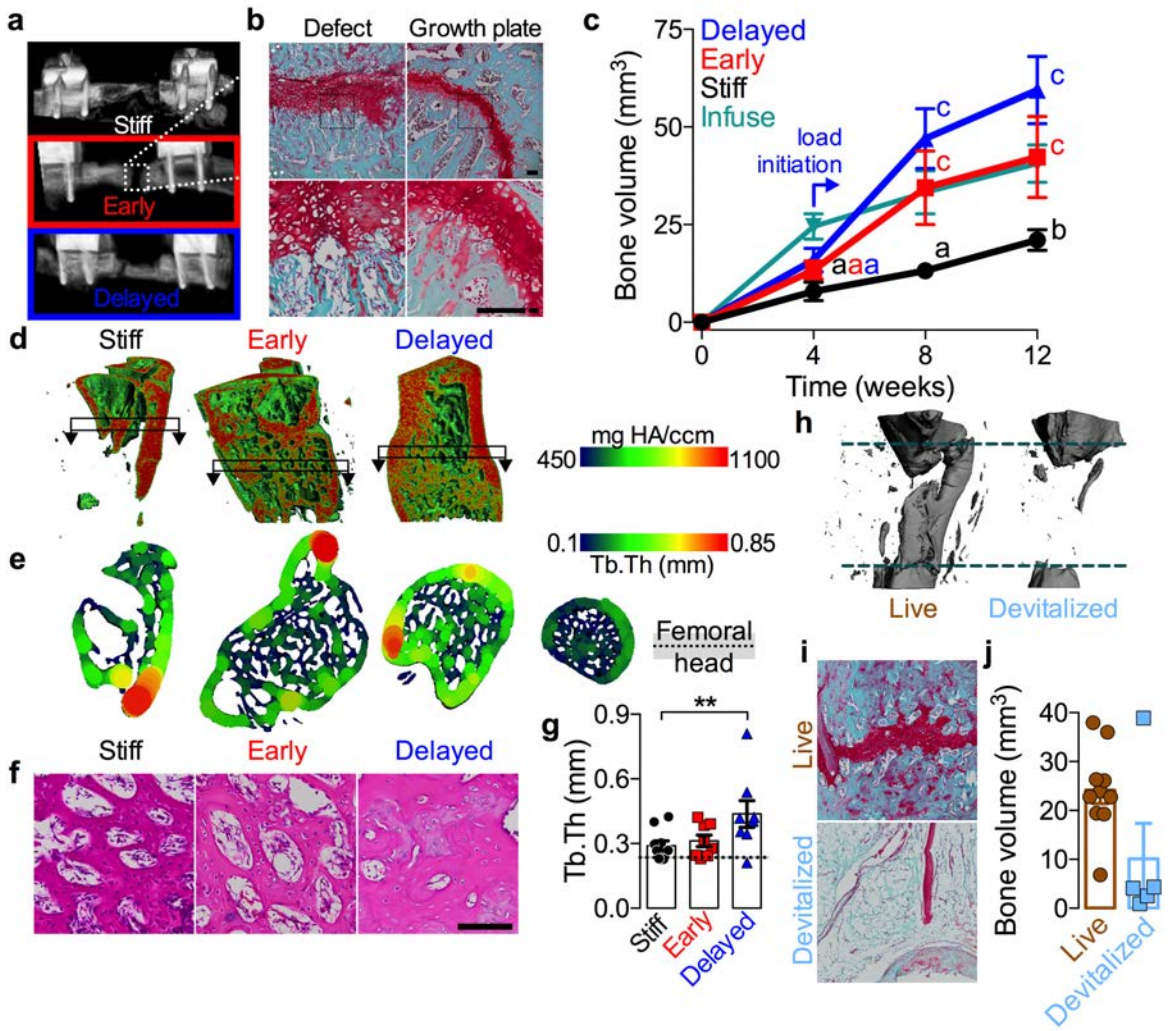

Figure 2: Mechanical loading enhances endochondral bone formation. a, *In vivo* microCT reconstructions at week 4 of bone defects implanted with engineered mesenchymal condensations and stabilized by stiff, early loading, or delayed loading fixation plates. Images selected based on mean bone volume at week 12. **b**, Safranin-O/Fast green staining of sagittal histological sections of defects at week 4 (left) demonstrating zonal cartilage and new woven bone, mimicking endochondral ossification in the native proximal femur growth plate (right). Bottom: magnification of enclosed areas. **c**, Longitudinal microCT quantification of bone volume at week 4 (n = 11, 11, 9, and 8 for stiff, early, and delayed, and infuse, respectively), week 8 (n = 10, 9, 8, 8) and 12 (n = 10, 8, 8, 8) demonstrating significantly increased endochondral bone formation in response to both early and delayed loading. The "Infuse" group featured 5µg rhBMP-2 delivered on absorbable collagen sponge. Infuse samples were performed at a separate time and were therefore not statistically compared. Filled data points indicate bridged samples, while open data points indicate non-bridged samples at each time point. **d**,

bioRxiv preprint doi: https://doi.org/10.1101/157362; this version posted June 29, 2017. The copyright holder for this preprint (which was not certified by peer review) is the author/funder, who has granted bioRxiv a license to display the preprint in perpetuity. It is made available under aCC-BY-NC-ND 4.0 International license.

Representative 3D microCT reconstructions at week 12 with local density mapping on sagittal virtual cut planes showing mineral concentration in a cortical shell. **e**, Representative microCT images of virtual transverse sections, as indicated by arrows in (**d**), with local trabecular thickness mapping, showing trabecular architecture similar to the native bone of the rat femoral head (right). **f**, H&E-stained histological sections at week 4 showing trabecular-like architecture of nascent osteocyte-populated bone (n = 1 representative sample per group selected based on mean bone volume at week 4). **g**, MicroCT-based morphometry analysis at week 12 of trabecular thickness within the cortical shell (n=10, 8, 8), demonstrating quantitative similarity with the trabecular morphology of the native femoral head, whose mean ± s.d. are shown as dotted line and shaded gray region. **h**, Representative microCT reconstructions showing defect region (between dotted red lines) with reduced bone formation beyond medullary canal capping in the devitalized group; images chosen based on mean bone volume. **i**, Representative histological staining of live and devitalized samples with Safranin-O/Fast green at week 12 showing fibrovascular tissue filling the defect in the devitalized group (n = 1 per group chosen based on mean bone volume at week 12). **j**, Bone volume at week 12 in live and devitalized groups. (n=10, 5). Scale bars, 100 µm. All data shown with mean ± s.e.m. *$p<0.05$, ** $p<0.01$, **** $p<0.0001$, NS = not significant, one or two-way ANOVA with Tukey's *post-hoc* analysis.

The principal test of any engineered tissue must be functional; therefore, to assess restoration of mechanical properties, we tested the limbs in torsion to failure at week 12 in comparison to age-matched intact femurs. Despite enhanced bone formation, early loading failed to recover mechanical properties at week 12 due to the low bridging rate. However, delayed loading significantly increased torsional stiffness and maximum torque compared to stiff plate controls (Fig. 3a,b y-axes) and restored the stiffness to that of intact limbs (dotted line). The corresponding structural properties, average polar moment of inertia (pMOI) and minimim pMOI (Fig. 3a,b x-axes) were also significantly elevated by delayed loading. To determine whether loading altered intrinsic mechanical properties independent of changes in geometry and bone distribution, we performed an analysis of covariance (ANCOVA) by regression analysis of the extrinsic properties, stiffness and maximum torque, against the corresponding moments of inertia. Differences in the best-fit regression lines would be indicative of changes in

bioRxiv preprint doi: https://doi.org/10.1101/157362; this version posted June 29, 2017. The copyright holder for this preprint (which was not certified by peer review) is the author/funder, who has granted bioRxiv a license to display the preprint in perpetuity. It is made available under aCC-BY-NC-ND 4.0 International license.

intrinsic mechanical properties after accounting for bone geometry. For both early and delayed groups, we found that loading increased intrinsic tissue mechanical properties. Thus, mechanical cues are critical for restoration of bone form and function to large defects by endochondral ossification.

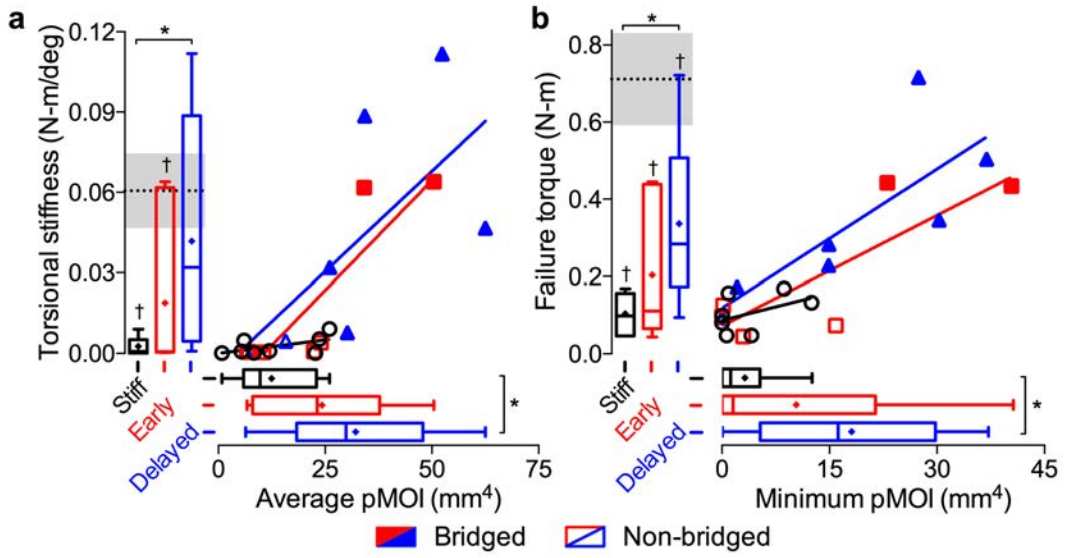

Figure 3: Restoration of mechanical function. a, Torsional stiffness (y-axis), shown with age-matched intact bone properties (dotted line/shading: mean ± s.d.), average polar moment of inertia (pMOI, x-axis), and scatter plot with correlation analysis (n = 8, 7, 7 for stiff, early, and delayed, respectively, $R^2_{stiff} = 0.34$, $R^2_{early} = 0.76$, $R^2_{delayed} = 0.45$). Delayed mechanical loading significantly enhanced torsional stiffness compared to stiff controls and restored stiffness to that of intact bone ($p<0.05$ vs. intact indicated by †). **b**, Maximum torque at failure with age-matched intact bone properties, graphed with minimum pMOI, and scatter plot with correlation analysis ($R^2_{stiff} = 0.21$, $R^2_{early} = 0.69$, $R^2_{delayed} = 0.63$). Delayed loading significantly increased failure torque compared to stiff controls. Box plots show interquartile range with whiskers at minimum and maximum values, center lines at median, and + symbols at the mean. Filled data points indicate bridged samples, while open data points indicate non-bridged samples. Scale bars, 100μm. Statistical comparisons between groups were performed by one-way ANOVA with Tukey's *post-hoc* analyses, *$p<0.05$.

To determine whether loading regulated endochondral lineage progression and matrix organization,[11,32] we performed histological staining at weeks 3, 4, 7, and 12 (Fig. 4a,b, Extended Data Figs. 4, 6, 7). Endochondral defects contained distinct bands of cartilage exhibiting mature and

bioRxiv preprint doi: https://doi.org/10.1101/157362; this version posted June 29, 2017. The copyright holder for this preprint (which was not certified by peer review) is the author/funder, who has granted bioRxiv a license to display the preprint in perpetuity. It is made available under aCC-BY-NC-ND 4.0 International license.

hypertrophic chondrocytes with prominent Safranin-O-stained matrix embedded in new woven bone, with extensive sGAG staining at early time points (Extended Data Figs. 4, 7) and calcified cartilage and bone at week 12 (Fig. 4a). Both early and delayed loading enhanced and prolonged the chondral phase of endochondral ossification, as indicated by Safranin-O staining intensity (Fig. 4a, Extended Data Figs. 4, 7). Polarized light analysis of picrosirius red-stained sections[11] revealed no differences in collagen organization during the initial healing period (Extended Data Fig. 6), but both early and delayed loading decreased collagen fiber birefringence compared to the stiff controls at week 12 (Fig. 4b), suggesting a persistence of immature woven bone in the loaded groups.

To further elucidate the transplanted cell fate and function, live human cells were immunolocalized by human nuclear antigen (HuNu) staining.[27] Remarkably, we observed viable human cells, morphologically identifiable as mature and hypertrophic chondrocytes (Fig. 4c), actively engaged in endochondral ossification as late as week 12 *in vivo*. These human cells also exhibited nuclear-localized YAP protein and expression of the downstream angiogenic matricellular growth factor, CYR61 (Fig. 4c). These observations together support the conclusion that the transplanted human cells engaged in endochondral lineage progression and mechanosensitive gene activity.

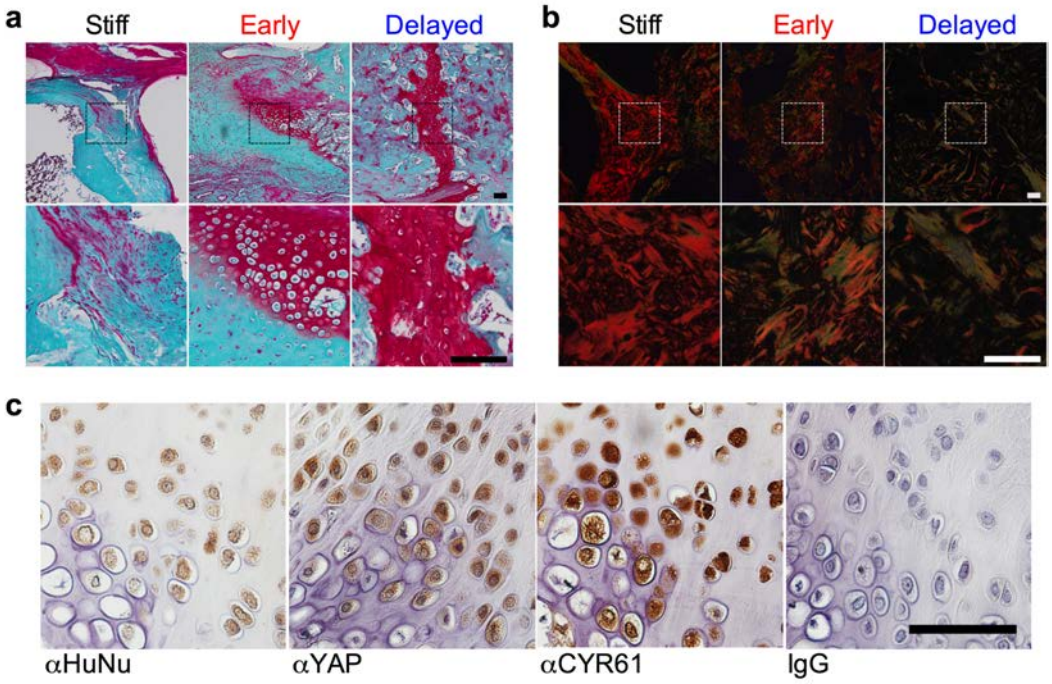

bioRxiv preprint doi: https://doi.org/10.1101/157362; this version posted June 29, 2017. The copyright holder for this preprint (which was not certified by peer review) is the author/funder, who has granted bioRxiv a license to display the preprint in perpetuity. It is made available under aCC-BY-NC-ND 4.0 International license.

Figure 4: Endochondral ossification, matrix remodeling, and transplanted cell engraftment. a, Safranin-O/Fast green staining of sagittal histological sections of defects at week 12 showing fibrocartilage and hypertrophic cartilage in the stiff and early groups and remnants of hypertrophic growth plate-like cartilage embedded in mineralized bone in the delayed group (n = 1 representative sample per group selected based on mean bone volume at week 12). **b**, Polarized light microscopy of picrosirius red-stained histological sections at week 12 showing reduced collagen fiber organization indicative of woven bone in the delayed group. **c**, Immunohistochemistry of live-cell treated, delayed loaded defects at week 12 demonstrating viable transplanted cells, positive for human nuclear antigen (HuNu), undergoing endochondral ossification and expressing YAP and downstream target gene CYR61. Right: isotype IgG negative control. Scale bar, 100 μm.

Angiogenesis enhances and accelerates the initiation of ossification in endochondral bone formation,[39,40] and is influenced by mechanical cues during bone defect repair.[10] To quantify vascular invasion of the cartilage anlage in response to mechanical loading, we used microCT angiography[41] to quantify the 3D blood vessel networks in and around the defect, three weeks after the onset of loading for both early (n = 10) and delayed (n = 8) loading, in comparison to contralateral stiff plate controls (n = 10, 8, respectively). Early loading did not alter bone formation at week 3, but significantly inhibited vascular ingrowth, blunting the preferentially axial orientation of the vessel network observed in the stiff group (Fig. 5a-g). Loading did not alter the vascular structures of the peripheral muscle, indicating a local effect of loading on angiogenic invasion or neovessel integrity (Extended Data Fig. 8a-d). Delayed loading enhanced bone formation at week 7 (Fig. 5h,j), consistent with our independent findings in Figure 2, but did not alter vascular morphometry parameters other than reduced vessel anisotropy (Fig. 5k-n) (Extended Data Fig. 8e-h).

In development, the cartilage anlage initiates as an avascular template that, upon chondrocyte hypertrophy, is invaded by blood vessels from the surrounding tissue. To test for this in the endochondral defects, we performed a region-of-interest (ROI) analysis, evaluating the vasculature at the defect core (1.5mm diameter) and in the surrounding annular region (5mm outer diameter). As

bioRxiv preprint doi: https://doi.org/10.1101/157362; this version posted June 29, 2017. The copyright holder for this preprint (which was not certified by peer review) is the author/funder, who has granted bioRxiv a license to display the preprint in perpetuity. It is made available under aCC-BY-NC-ND 4.0 International license.

hypothesized, the core region remained distinctly avascular (Figure 6a,d), and coincident with cartilage matrix observed histologically (Extended Data Fig. 7). This avascular core was not present at the 3 and 7 week time points in prior studies with BMP-2 delivery, which induced regeneration primarily through intramembranous ossification,[10] suggesting this may be specific to endochondral repair.

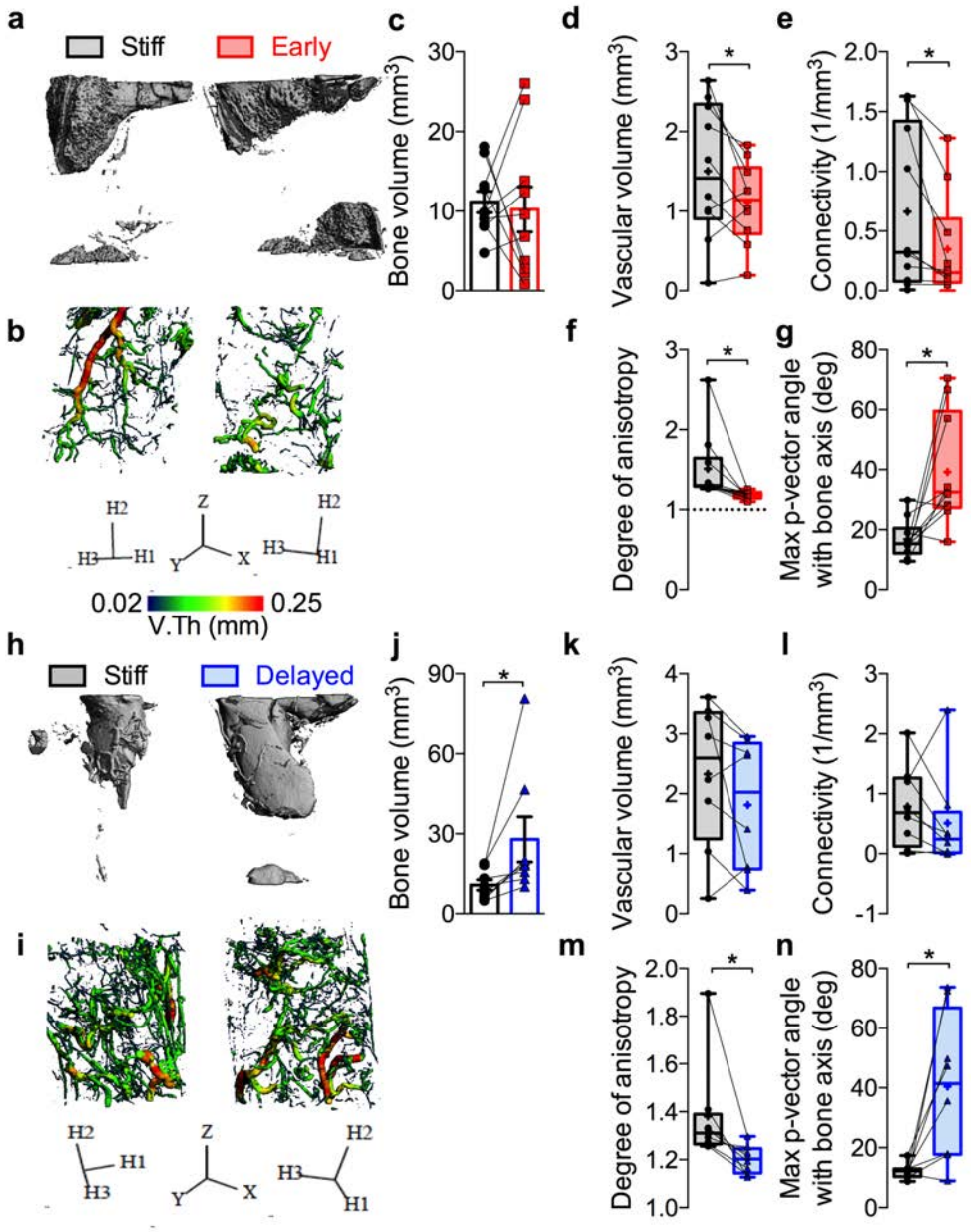

Figure 5: Mechanical control of neovascularization. a-b, Representative microCT reconstructions of bone (**a**) and blood vessels with local vessel diameter mapping (**b**) under stiff and early loading conditions at week 3, n = 10 . Images selected based on mean vessel volume. **c**, Early loading did not affect bone volume at week 3 in paired limbs with contralateral controls. **d-**

bioRxiv preprint doi: https://doi.org/10.1101/157362; this version posted June 29, 2017. The copyright holder for this preprint (which was not certified by peer review) is the author/funder, who has granted bioRxiv a license to display the preprint in perpetuity. It is made available under aCC-BY-NC-ND 4.0 International license.

g, Three-dimensional vascular network morphometry demonstrating reduced vascular volume (**d**) and connectivity (**e**) and altered vessel orientation and distribution in early-loaded defects ($p<0.05$, paired two-tailed Student's t-test), as measured by degree of anisotropy (**f**) and the angle with respect to the bone-axis of the maximum principal eigenvector (H2) of the mean intercept length (MIL) tensor, indicating the dominant direction of vessel orientation. Degree of anisotropy represents the ratio of the longest and shortest MIL eigenvalues. DA=1 (dotted line) indicates isotropy. **h-i,** Representative microCT reconstructions of bone (**h**) and blood vessels with local vessel diameter mapping (**i**) under stiff and early loading conditions at week 7, n = 8. **j**, Delayed loading significantly enhanced bone volume in paired limbs with contralateral controls. **k-n**, However, delayed loading did not significantly alter vascular network morphometry as measured by vascular volume (**k**), connectivity (**l**), degree of anisotropy (**m**) or maximum principal vector angle (**n**). Paired data are shown superimposed on box plots displaying median as horizontal line, inter-quartile range as boxes, and min/max range as whiskers. Mean values are indicated by +.

As blood vessel invasion of the cartilage anlage is essential to initiate cartilage remodeling and ossification,[42] we next sought to determine the amount and spatial distribution of cartilaginous matrix in the regions of low and high vascularity and whether loading influenced 3D cartilage distribution. We incubated the post-decalcified, vasculature-perfused defects with the X-ray-attenuating cationic contrast agent, CA^{4+}), which partitions at equilibrium with the negatively charged sulfated glycosaminoglycans (sGAG) of the endochondral cartilage matrix and attenuates X-rays proportional to sGAG concentration.[43] CA^{4+}-partitioned cartilage was moderately concentrated in the avascular core, but was also present throughout the defect. While early loading produced a trend of increased cartilage content in both the annular and core regions, differences between loading groups did not reach statistical significance (Fig. 6f-h).

Thus, we conclude that the large deformations associated with early loading inhibited axial blood vessel integrity or neovascular invasion of the cartilage anlage, yielding an avascular core, consistent with recent observations of phenotypic stability of MSC-derived chondrocytes *in vivo* by inhibition of

bioRxiv preprint doi: https://doi.org/10.1101/157362; this version posted June 29, 2017. The copyright holder for this preprint (which was not certified by peer review) is the author/funder, who has granted bioRxiv a license to display the preprint in perpetuity. It is made available under aCC-BY-NC-ND 4.0 International license.

angiogenesis,[44] but permitted transverse vessel recruitment to facilitate the progression of endochondral ossification.

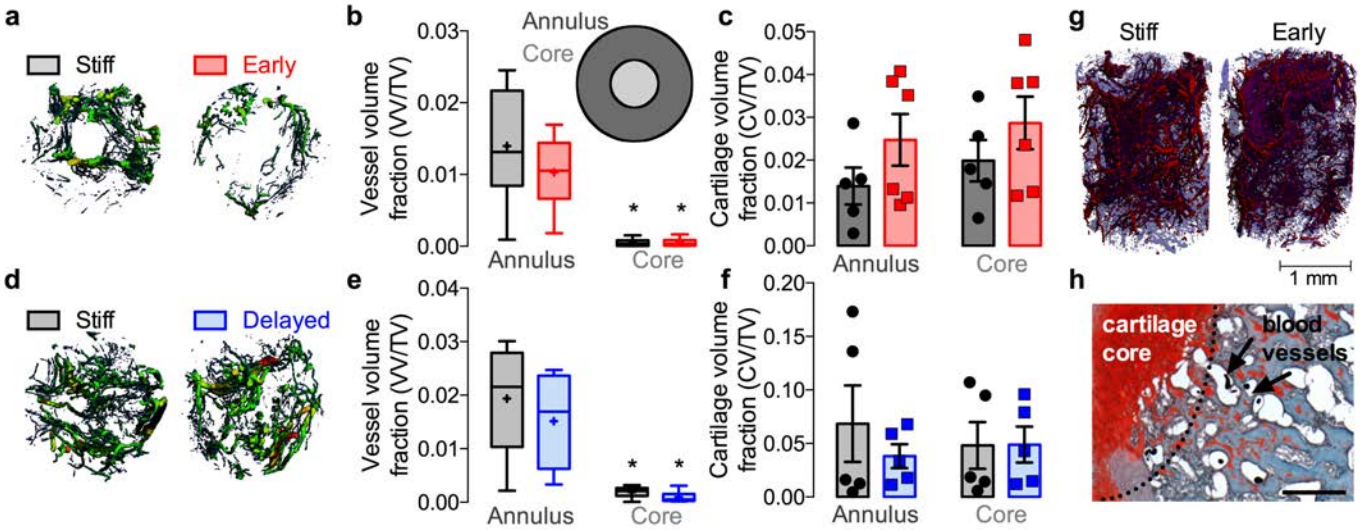

Figure 6: Spatial distribution of neovascular and cartilaginous tissues. a, 3D neovessel diameter mapping under stiff and early loading conditions at week 3, n = 10. Images selected based on mean vessel volume. **b**, Region of interest analysis demonstrating significantly reduced vascular volume fraction in the 1.5mm diameter core compared to the 5mm-1.5mm annular region (inset; $p<0.05$, two-way ANOVA with Tukey's *post-hoc* comparisons). Box plots display median as horizontal line, inter-quartile range as boxes, and min/max range as whiskers. Mean values are indicated by +. **c**, Cationic (CA^{4+}) cartilage contrast-enhanced microCT quantification of cartilage in annulus and core regions. Data points shown with mean ± s.e.m. n = 5-6. **d**, 3D neovessel diameter mapping under stiff and delayed loading conditions at week 7, n = 8. **e**, Region of interest analysis demonstrating significantly reduced vascular volume fraction in the 1.5mm diameter core compared to the 5mm-1.5mm annular region (inset; $p<0.05$, two-way ANOVA with Tukey's *post-hoc* comparisons). Box plots display median as horizontal line, inter-quartile range as boxes, and min/max range as whiskers. Mean values are indicated by +. **f**, Cationic (CA^{4+}) cartilage contrast-enhanced microCT quantification of cartilage in annulus and core regions. Data points shown with mean ± s.e.m. n = 5-6. **g**, representative images of co-registered contrast enhanced cartilage imaging by CA^{4+}) (transparent blue) with microCT angiography of neovasculature (opaque red). **h**, Safranin-O/Fast green-stained histological sections of vascular contrast agent-perfused tissues demonstrated bone formation, endochondral ossification, and patent microvasculature. Residual contrast agent exhibits thermal contraction

bioRxiv preprint doi: https://doi.org/10.1101/157362; this version posted June 29, 2017. The copyright holder for this preprint (which was not certified by peer review) is the author/funder, who has granted bioRxiv a license to display the preprint in perpetuity. It is made available under aCC-BY-NC-ND 4.0 International license.

during histological paraffin processing, visible as dark dots in vessel lumens. **d**, Representative images of co-registered cartilage and vascular structures. Scale bar, 100 μm.

Collectively, this study presents a human progenitor cell-based tissue engineering approach that recapitulates developmental cell-cell organization and differentiation through engineered hMSC condensations with local morphogen presentation through biodegradable biopolymer microspheres and *in vivo* control of mechanical forces. These findings demonstrate the importance of *in vivo* mechanical stimuli and controlled morphogen presentation for functional, vascularized tissue regeneration through endochondral ossification and implicate mechanical cues as important factors for successful biomimetic tissue engineering of other tissues whose form and function is dictated by mechanical stimuli during development and homeostasis.

Limitations

These used athymic (RNU) rats to facilitate xenogenic implantation and assessment of functional hMSC engraftment,[27] but this model may miss some immunomodulatory functions of the transplanted cells.[45] However, potential translational application of these findings to the clinic would likely involve autologous cell transplantation which would not illicit a T-cell response. This makes the RNU a reasonable model for this approach.[27] Additionally, the rnu/rnu strain maintains an intact thymus-independent immune response including natural killer cells,[45] which are known to be inhibited by MSCs,[45] suggesting that some of the immunomodulatory function may be maintained in this model. A detailed exploration of hMSC-immune cell interactions has not been performed under the endochondral paradigm and warrants investigation, but is outside the scope of the present study.

The model used in these studies features bilateral defects, with compliant (early or delayed) and stiff plates distributed in either of two ways: 1) evenly distributed among limbs such that each fixation plate is paired with each other type in equal numbers, or 2) each ipsilateral compliant plate (early or delayed) is paired with a contralateral stiff fixation plate. This design is used for two reasons. First, it enables accounting for animal-animal variability and microfil perfusion quality in statistical models. Second,

bioRxiv preprint doi: https://doi.org/10.1101/157362; this version posted June 29, 2017. The copyright holder for this preprint (which was not certified by peer review) is the author/funder, who has granted bioRxiv a license to display the preprint in perpetuity. It is made available under aCC-BY-NC-ND 4.0 International license.

should preferential weight bearing cause reduced loading of the limbs that are affixed with compliant plates, this preferential unloading would be further exacerbated if the contralateral limb were unoperated. In prior experiments, we have verified that there are no systemic or contralateral effects of hMSC transplantation[27] or growth factor presentation[4] for both bone formation and angiogenesis[10,46]. In this study, we observe no differences in bone formation in the ipsilateral limb based on fixation plate type on the contralateral limb, suggesting that ambulatory imbalance is low or not sufficient to alter load-induced bone regeneration. Daily observation of animal ambulation and *in vivo* x-ray videography[30,47] during treadmill ambulation demonstrate that compliant plates do not impair weight bearing in either limb during ambulation. Further, we previously evaluated gait kinematics in response to fixation plate insertion and bone defect creation and found no significant differences between groups or compared to sham-operated controls, indicating that defect creation and fixation implantation does not significantly alter gait kinematics.[48]

Methods

Methods are available in the online version of the paper.

Competing interests

The authors declare they have no competing financial interests.

Acknowledgements

We thank the staff of the Freimann Life Science Center (FLSC) at the University of Notre Dame for animal care and husbandry, the staff of the Notre Dame Integrated Imaging Facility (NDIIF) for imaging support, and Amad Awadallah of the Case Western Reserve University Histology Core Facility for technical support. We thank Glen Niebur, University of Notre Dame, for insightful comments on the manuscript. We gratefully acknowledge funding from the Naughton Foundation (A.M.M., J.D.B.), the Indiana Clinical and Translational Sciences Institute, grant number UL1TR001108 from the National Institutes of Health (J.D.B), the American Heart Association, grant number 16SDG31230034 (J.D.B), the National Institutes of Health's National Institute of Arthritis and Musculoskeletal and Skin Diseases

bioRxiv preprint doi: https://doi.org/10.1101/157362; this version posted June 29, 2017. The copyright holder for this preprint (which was not certified by peer review) is the author/funder, who has granted bioRxiv a license to display the preprint in perpetuity. It is made available under aCC-BY-NC-ND 4.0 International license.

under award number R01AR063194 (E.A.), the National Institutes of Health's National Institute of Dental and Craniofacial Research under award number 5F32DE024712 (S.H.), and the Ohio Biomedical Research Commercialization Program under award number TECG20150782 (E.A.). The contents of this publication are solely the responsibility of the authors and do not necessarily represent the official views of the National Institutes of Health or other funding agency.

Author contributions

E.A. and J.D.B. conceived and supervised the research. A.M.M., S.H., E.A., and J.D.B. designed the experiments, analyzed the data, and wrote the paper. All authors collected data, and commented on and approved the final manuscript. Correspondence and requests for materials should be addressed to E.A. (exa46@case.edu) or J.D.B. (jboercke@nd.edu).

bioRxiv preprint doi: https://doi.org/10.1101/157362; this version posted June 29, 2017. The copyright holder for this preprint (which was not certified by peer review) is the author/funder, who has granted bioRxiv a license to display the preprint in perpetuity. It is made available under aCC-BY-NC-ND 4.0 International license.

REFERENCES

1. Gerstenfeld, L. C., Cullinane, D. M., Barnes, G. L., Graves, D. T. & Einhorn, T. a. Fracture healing as a post-natal developmental process: molecular, spatial, and temporal aspects of its regulation. *J. Cell. Biochem.* **88,** 873–84 (2003).
2. Pountos, I., Georgouli, T., Pneumaticos, S. & Giannoudis, P. V. Fracture non-union: Can biomarkers predict outcome? *Injury* **44,** 1725–32 (2013).
3. Jones, A. L. *et al.* Recombinant human BMP-2 and allograft compared with autogenous bone graft for reconstruction of diaphyseal tibial fractures with cortical defects. A randomized, controlled trial. *J. Bone Joint Surg. Am.* **88,** 1431–41 (2006).
4. Boerckel, J. D. *et al.* Effects of protein dose and delivery system on BMP-mediated bone regeneration. *Biomaterials* **32,** 5241–51 (2011).
5. Hamburger, V. & Waugh, M. The Primary Development of the Skeleton in Nerveless and Poorly Innervated Limb Transplants of Chick Embryos. *Physiol. Zool.* **13,** 367–382 (1940).
6. Hosseini, a & Hogg, D. a. The effects of paralysis on skeletal development in the chick embryo. I. General effects. *J. Anat.* **177,** 159–168 (1991).
7. Kenwright, J. *et al.* Effect of controlled axial micromovement on healing of tibial fractures. *Lancet (London, England)* **2,** 1185–7 (1986).
8. Goodship, A. E. & Kenwright, J. The influence of induced micromovement upon the healing of experimental tibial fractures. *J. Bone Joint Surg. Br.* **67,** 650–5 (1985).
9. Claes, L., Eckert-Hübner, K. & Augat, P. The effect of mechanical stability on local vascularization and tissue differentiation in callus healing. *J. Orthop. Res.* **20,** 1099–105 (2002).
10. Boerckel, J. D., Uhrig, B. a, Willett, N. J., Huebsch, N. & Guldberg, R. E. Mechanical regulation of vascular growth and tissue regeneration in vivo. *Proc. Natl. Acad. Sci. U. S. A.* **108,** E674-80 (2011).
11. Boerckel, J. D. *et al.* Effects of in vivo mechanical loading on large bone defect regeneration. *J. Orthop. Res.* **30,** 1067–75 (2012).
12. Glatt, V. *et al.* Improved healing of large segmental defects in the rat femur by reverse dynamization in the presence of bone morphogenetic protein-2. *J. Bone Joint Surg. Am.* **94,** 2063–73 (2012).
13. Lefebvre, V. & Bhattaram, P. Vertebrate skeletogenesis. *Curr. Top. Dev. Biol.* **90,** 291–317 (2010).
14. Claes, L. E. *et al.* Effects of mechanical factors on the fracture healing process. *Clin.Orthop.Relat Res* **355S,** S132–S147 (1998).
15. Lacroix, D. & Prendergast, P. J. A mechano-regulation model for tissue differentiation during fracture healing: analysis of gap size and loading. *J. Biomech.* **35,** 1163–1171 (2002).
16. Ingber, D. E. *et al.* Tissue engineering and developmental biology: going biomimetic. *Tissue Eng.* **12,** 3265–83 (2006).
17. Alsberg, E., Anderson, K. W., Albeiruti, A., Rowley, J. A. & Mooney, D. J. Engineering growing tissues. *Proc. Natl. Acad. Sci. U. S. A.* **99,** 12025–12030 (2002).
18. Solorio, L. D., Vieregge, E. L., Dhami, C. D., Dang, P. N. & Alsberg, E. Engineered cartilage via self-assembled hMSC sheets with incorporated biodegradable gelatin microspheres releasing transforming growth factor-β1. *J. Control. Release* **158,** 224–32 (2012).
19. McDermott, A. M., Mason, D. E., Lin, A. S. P., Guldberg, R. E. & Boerckel, J. D. Influence of structural load-bearing scaffolds on mechanical load- and BMP-2-mediated bone regeneration. *J. Mech. Behav. Biomed. Mater.* **62,** 169–181 (2016).
20. Han, Y. & Lefebvre, V. L-Sox5 and Sox6 drive expression of the aggrecan gene in cartilage by securing binding of Sox9 to a far-upstream enhancer. *Mol. Cell. Biol.* **28,** 4999–5013 (2008).
21. Lefebvre, V., Huang, W., Harley, V. R., Goodfellow, P. N. & de Crombrugghe, B. SOX9 is a potent activator of the chondrocyte-specific enhancer of the pro alpha1(II) collagen gene. *Mol. Cell. Biol.* **17,** 2336–2346 (1997).
22. Dupont, S. *et al.* Role of YAP/TAZ in mechanotransduction. *Nature* **474,** 179–83 (2011).

bioRxiv preprint doi: https://doi.org/10.1101/157362; this version posted June 29, 2017. The copyright holder for this preprint (which was not certified by peer review) is the author/funder, who has granted bioRxiv a license to display the preprint in perpetuity. It is made available under aCC-BY-NC-ND 4.0 International license.

23. Pefani, D.-E. *et al.* TGF-β Targets the Hippo Pathway Scaffold RASSF1A to Facilitate YAP/SMAD2 Nuclear Translocation. *Mol. Cell* **63,** 156–166 (2016).
24. Kegelman, C. D. *et al.* Skeletal Cell YAP And TAZ Redundantly Promote Bone Development By Regulation Of Collagen I Expression And Organization. *bioRxiv* (2017).
25. Karystinou, A. *et al.* Yes-associated protein (YAP) is a negative regulator of chondrogenesis in mesenchymal stem cells. *Arthritis Res. Ther.* **17,** 1–14 (2015).
26. Kolambkar, Y. M. *et al.* An alginate-based hybrid system for growth factor delivery in the functional repair of large bone defects. *Biomaterials* **32,** 65–74 (2011).
27. Dupont, K. M. *et al.* Human stem cell delivery for treatment of large segmental bone defects. *Proc. Natl. Acad. Sci. U. S. A.* **107,** 3305–10 (2010).
28. Goodship, A. E., Cunningham, J. L. & Kenwright, J. Strain rate and timing of stimulation in mechanical modulation of fracture healing. *Clin. Orthop. Relat. Res.* S105-15 (1998).
29. Wehner, T. *et al.* Internal forces and moments in the femur of the rat during gait. *J. Biomech.* **43,** 2473–2479 (2010).
30. Klosterhoff, B. S. *et al.* Wireless Implantable Sensor For Non-Invasive, Longitudinal Quantification Of Axial Strain Across Rodent Long Bone Defects. *bioRxiv* (2017).
31. Chandaria, V. V., McGinty, J. & Nowlan, N. C. Characterising the effects of in vitro mechanical stimulation on morphogenesis of developing limb explants. *J. Biomech.* **49,** 3635–3642 (2016).
32. Palomares, K. T. S. *et al.* Mechanical stimulation alters tissue differentiation and molecular expression during bone healing. *J. Orthop. Res.* **27,** 1123–32 (2009).
33. McKay, W. F., Peckham, S. M. & Badura, J. M. A comprehensive clinical review of recombinant human bone morphogenetic protein-2 (INFUSE?? Bone Graft). *Int. Orthop.* **31,** 729–734 (2007).
34. Freeman, F. E., Allen, A. B., Stevens, H. Y., Guldberg, R. E. & McNamara, L. M. Effects of in vitro endochondral priming and pre-vascularisation of human MSC cellular aggregates in vivo. *Stem Cell Res. Ther.* **6,** 218 (2015).
35. Scotti, C. *et al.* Recapitulation of endochondral bone formation using human adult mesenchymal stem cells as a paradigm for developmental engineering. *Proc. Natl. Acad. Sci. U. S. A.* **107,** 7251–6 (2010).
36. Bahney, C. S. *et al.* Stem Cell–Derived Endochondral Cartilage Stimulates Bone Healing by Tissue Transformation. *J. Bone Miner. Res.* **29,** 1269–1282 (2014).
37. Yang, L., Tsang, K. Y., Tang, H. C., Chan, D. & Cheah, K. S. Hypertrophic chondrocytes can become osteoblasts and osteocytes in endochondral bone formation. *Proc. Natl. Acad. Sci. U. S. A.* **111,** 12097–12102 (2014).
38. Zhou, X. *et al.* Chondrocytes transdifferentiate into osteoblasts in endochondral bone during development, postnatal growth and fracture healing in mice. *PLoS Genet.* **10,** e1004820 (2014).
39. Ramasamy, S. K., Kusumbe, A. P., Wang, L. & Adams, R. H. Endothelial Notch activity promotes angiogenesis and osteogenesis in bone. *Nature* **507,** 376–380 (2014).
40. Gerber, H.-P. *et al.* VEGF couples hypertrophic cartilage remodeling, ossification and angiogenesis during endochondral bone formation. *Nat. Med.* **5,** 623–628 (1999).
41. Boerckel, J. D., Mason, D. E., McDermott, A. M. & Alsberg, E. Microcomputed tomography: approaches and applications in bioengineering. *Stem Cell Res. Ther.* **5,** 144 (2014).
42. Ferrara, N. *et al.* VEGF couples hypertrophic cartilage remodeling, ossification and angiogenesisduring endochondral bone formation. *Nat. Med.* **5,** 623–628 (1999).
43. Hayward, L. N. M., De Bakker, C. M. J., Gerstenfeld, L. C., Grinstaff, M. W. & Morgan, E. F. Assessment of contrast-enhanced computed tomography for imaging of cartilage during fracture healing. *J. Orthop. Res.* **31,** 567–573 (2013).
44. Marsano, A. *et al.* Spontaneous In Vivo Chondrogenesis of Bone Marrow-Derived Mesenchymal Progenitor Cells by Blocking Vascular Endothelial Growth Factor Signaling. *Stem Cells Transl. Med.* sctm-2015 (2016).

bioRxiv preprint doi: https://doi.org/10.1101/157362; this version posted June 29, 2017. The copyright holder for this preprint (which was not certified by peer review) is the author/funder, who has granted bioRxiv a license to display the preprint in perpetuity. It is made available under aCC-BY-NC-ND 4.0 International license.

45. Gotherstrom, C., Ringden, O., Westgren, M., Tammik, C. & Le Blanc, K. Immunomodulatory effects of human foetal liver-derived mesenchymal stem cells. *Bone Marrow Transplant.* **32,** 265–272 (2003).
46. Kolambkar, Y. M. *et al.* Spatiotemporal delivery of bone morphogenetic protein enhances functional repair of segmental bone defects. *Bone* **49,** 485–492 (2011).
47. Boerckel, J. D., Dupont, K. M., Kolambkar, Y. M., Lin, A. S. P. & Guldberg, R. E. In vivo model for evaluating the effects of mechanical stimulation on tissue-engineered bone repair. *J. Biomech. Eng.* **131,** 84502 (2009).
48. Uhrig, B. A. *et al.* Characterization of a composite injury model of severe lower limb bone and nerve trauma. *J. Tissue Eng. Regen. Med.* **8,** 432–41 (2014).
49. Stewart, R. C. *et al.* Contrast-enhanced CT with a High-Affinity Cationic Contrast Agent for Imaging ex Vivo Bovine, Intact ex Vivo Rabbit, and in Vivo Rabbit Cartilage. *Radiology* **266,** 141–150 (2013).

bioRxiv preprint doi: https://doi.org/10.1101/157362; this version posted June 29, 2017. The copyright holder for this preprint (which was not certified by peer review) is the author/funder, who has granted bioRxiv a license to display the preprint in perpetuity. It is made available under aCC-BY-NC-ND 4.0 International license.

Extended Data

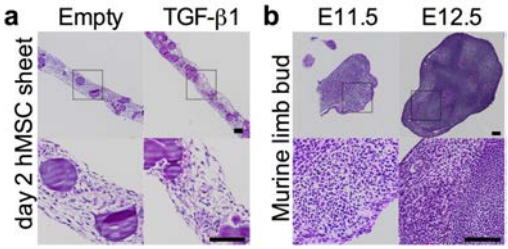

Extended Data Figure 1: H&E staining of mesenchymal condensations and murine embryonic limb buds. a, Haematoxylin and eosin (H&E) staining of hMSC sheets cultured for two days on transwell inserts with empty gelatin microspheres (left), or loaded with 600 ng TGF-β1 (right). Bottom: magnification of enclosed areas. **b**, H&E staining of murine limb buds at embryonic days 11.5 and 12.5 (E11.5, E12.5). Bottom: photomicrographs of embryos with limb buds indicated by arrows. Scale bars, 100 μm. Histological images are representative of 3 independent samples per group.

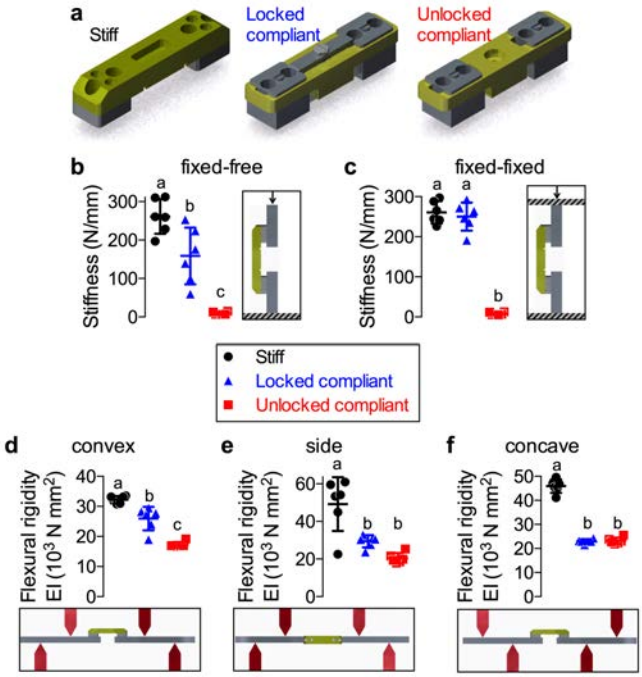

Extended Data Figure 2: Fixation plate characterization. a, Bilateral critically-sized (8 mm) defects in the femora of 14 week-old, male RNU rates were stabilized by fixation plates that enabled dynamic control of ambulatory load sharing (n = 6 per group). **b-c**, Axial compression testing with fixed-fixed or fixed-free boundary conditions, as illustrated. **d-f**, Four-point bend testing in three directions, as illustrated, with supports and load applied to maintain constant bending moment on the plate. Statistical comparisons evaluated by one-way ANOVA on log-transformed data to ensure normality of residuals followed by Tukey's *post hoc* test. Summary data shown as mean ± standard deviation.

bioRxiv preprint doi: https://doi.org/10.1101/157362; this version posted June 29, 2017. The copyright holder for this preprint (which was not certified by peer review) is the author/funder, who has granted bioRxiv a license to display the preprint in perpetuity. It is made available under aCC-BY-NC-ND 4.0 International license.

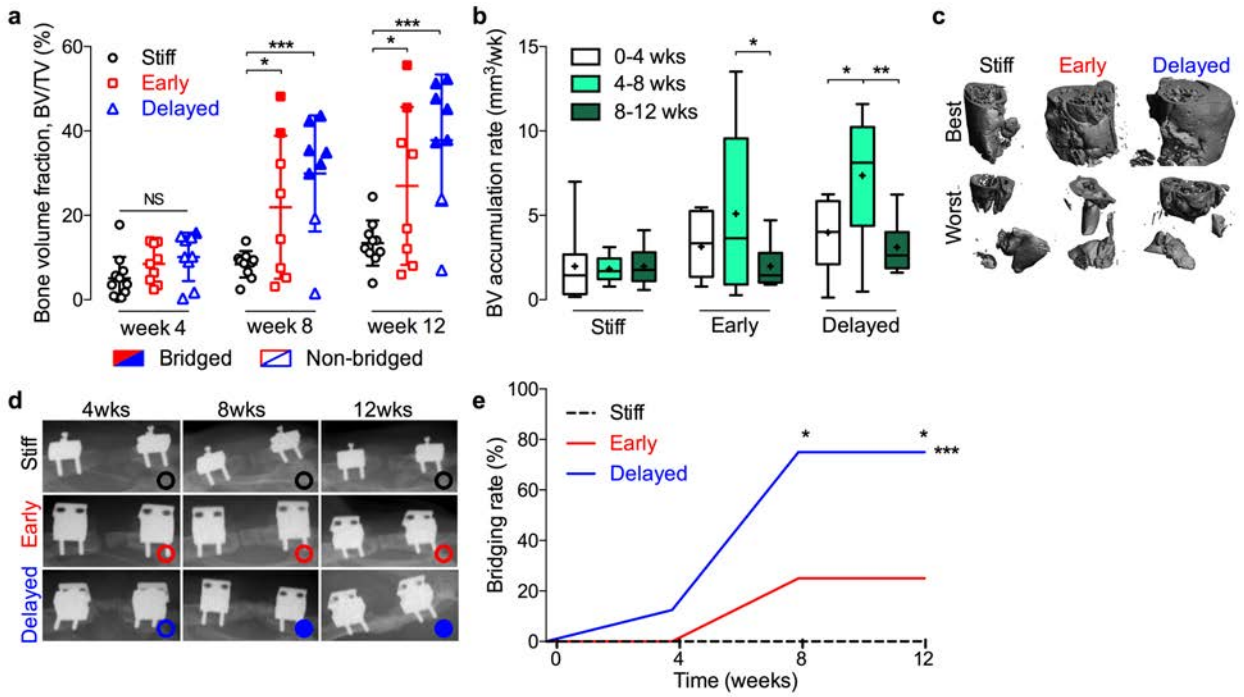

Extended Data Figure 3: Bone accumulation and bridging rates. a, Bone volume fraction (BV/TV) over time. Individual data points shown with mean ± s.d. Samples with bony bridging are shown in shaded data points, while open data points indicate non-bridged. **b**, accumulation rate, defined as bone volume accrual over each 4-week interval. Box plots display median as horizontal line, inter-quartile range as boxes, and min/max range as whiskers. Mean values are indicated by +. BV accumulation rate was elevated in both early and delayed groups between weeks 4 and 8. *p<0.05, **p<0.01, ***p<0.001, two-way ANOVA with Tukey's *post-hoc* analysis. **c**, High resolution (20 µm voxel size) MicroCT reconstructions of excised femurs at week 12 showing best- and worst-case regeneration for each group. **d.** Representative x-ray images for each group at 4, 8 and 12 weeks illustrating bridged (filled circles) and non-bridged (open circles) samples; images chosen based on mean bone volume at week 12. **e**, Longitudinal analysis of bone bridging *in vivo* at 4 (n= 11, 11, 9, for stiff, early, and delayed, respectively), 8 (n =10, 9, 8) and 12 weeks (n = 10, 8, 8) determined via x-ray as mineral fully traversing the defect. Significance of trend was analyzed by chi-square test for trend (***p<0.001) while differences between groups were determined by chi-square test at each time point with Bonferroni correction (*p<0.05). All stiff group samples failed to bridge by week 12, while 25% and 75% of the early and delayed loading groups achieved bridging by this time point, respectively.

bioRxiv preprint doi: https://doi.org/10.1101/157362; this version posted June 29, 2017. The copyright holder for this preprint (which was not certified by peer review) is the author/funder, who has granted bioRxiv a license to display the preprint in perpetuity. It is made available under aCC-BY-NC-ND 4.0 International license.

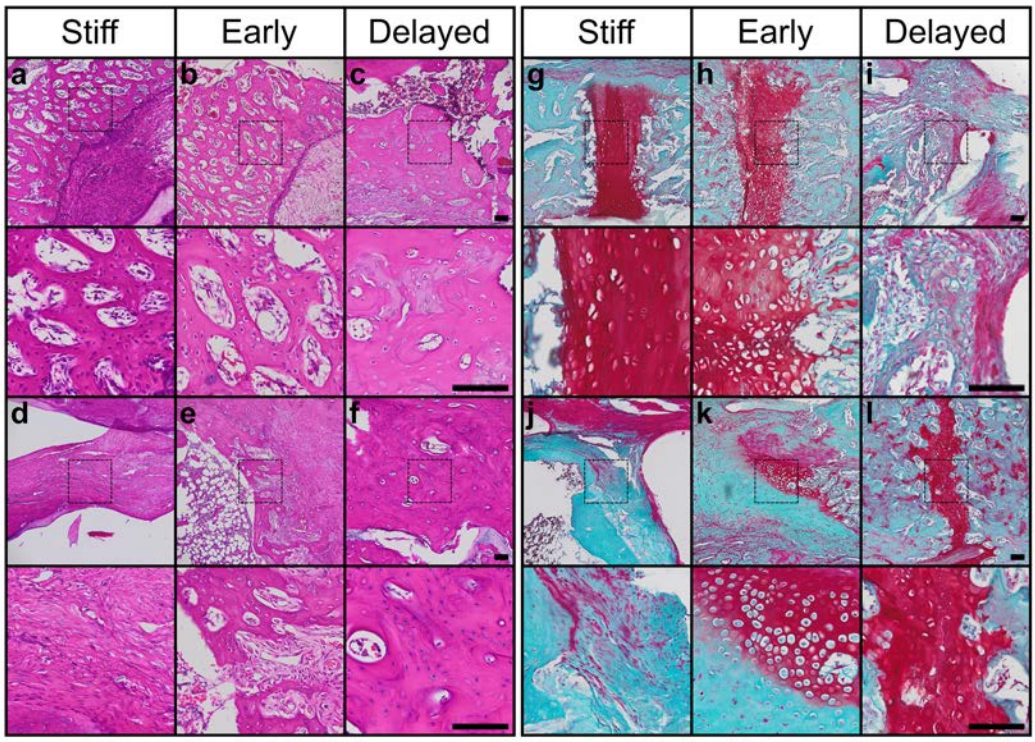

Extended Data Figure 4: Full histological analysis of endochondral bone formation. a-f, H&E staining. **g-I**, Safranin-O/Fast green staining at 10x (top) and 40x (bottom, magnification of dotted squares). Scale bars, 100 µm. Panels **a-c** and **g-I** show tissues at week 4 and panels **d-f** and **j-l** show tissues at week 12 (n = 1 per group at each time point, chosen by proximity to mean bone volume *in vivo* at 4 and 12 weeks). Bone formation in the defect exhibited porous trabecular morphology, though stiff and early groups exhibited some fibrotic and fibrocartilaginous tissue at week 12. Safranin-O staining revealed that non-mineralized bands observed in microCT reconstructions consisted of mature and hypertrophic chondrocytes, giving rise to woven and neotrabecular bone. The stiff and early groups exhibited fibrocartilage and hypertrophic cartilage at week 12. The delayed loading group had remnants of hypertrophic growth plate-like cartilage that was fused and embedded in mineralized bone.

bioRxiv preprint doi: https://doi.org/10.1101/157362; this version posted June 29, 2017. The copyright holder for this preprint (which was not certified by peer review) is the author/funder, who has granted bioRxiv a license to display the preprint in perpetuity. It is made available under aCC-BY-NC-ND 4.0 International license.

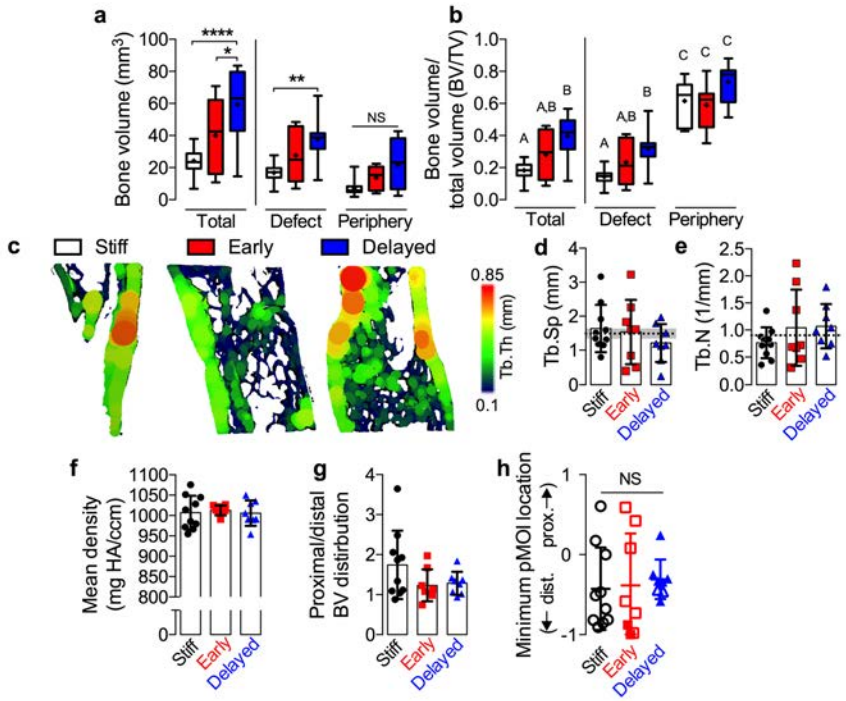

Extended Data Figure 5: MicroCT region of-interest analysis demonstrating formation of cortical and trabecular bone compartments. a, Region of interest (ROI) analyses of bone volume in total, defect, and periphery ROIs, defined by regions inside 5mm diameter cylinder or annulus with 7 mm outer diameter and 5 mm inner diameter (n = 10, 8, 8 for stiff, early, and delayed respectively). Delayed mechanical loading enhanced bone formation, especially in the defect ROI. **b**, ROI analysis of bone volume fraction. Groups with shared significance indicator letters have no significant differences. Bone was most concentrated in the ectopic region, indicative of a cortical shell, but differences between groups were most prominent in the defect region. Increased thickness in a cortex-like shell was evident in each group. **c**, Representative microCT images of sagittal sections with mean trabecular thickness mapping overlay; images selected based on mean bone volume. **d,e**, MicroCT-based morphometry analysis at week 12 (n=10, 8, 8) of trabecular number (**d**), and trabecular spacing (**e**) within the cortical shell demonstrating quantitative similarity with the trabecular morphology of the native femoral head, whose mean ± s.d. are shown as dotted line and shaded gray region. **f**, Mean mineral density. No differences between groups were detected. **g**, Proximal vs. distal region of interest analysis, expressed as ratio of bone volume in proximal to distal halves of the defect. Data showed a trend toward greater bone formation in the proximal half of the defect, especially in the stiff plate group. **h**, The location of minimum pMOI for each sample, with mean ± s.d. In panel **h**, filled data points indicate bridged samples and open data points indicate non-bridged samples. Box plots show interquartile range with whiskers at minimum and maximum values, center lines at median, and + symbols at the mean. Bar graphs show data with mean ± s.d. Dotted lines with shaded gray regions indicate mean ± s.d. of intact bone properties. *p<0.05, ** p<0.01, **** p<0.0001, NS = not significant, one or two-way ANOVA with Tukey's *post-hoc* analysis.

bioRxiv preprint doi: https://doi.org/10.1101/157362; this version posted June 29, 2017. The copyright holder for this preprint (which was not certified by peer review) is the author/funder, who has granted bioRxiv a license to display the preprint in perpetuity. It is made available under aCC-BY-NC-ND 4.0 International license.

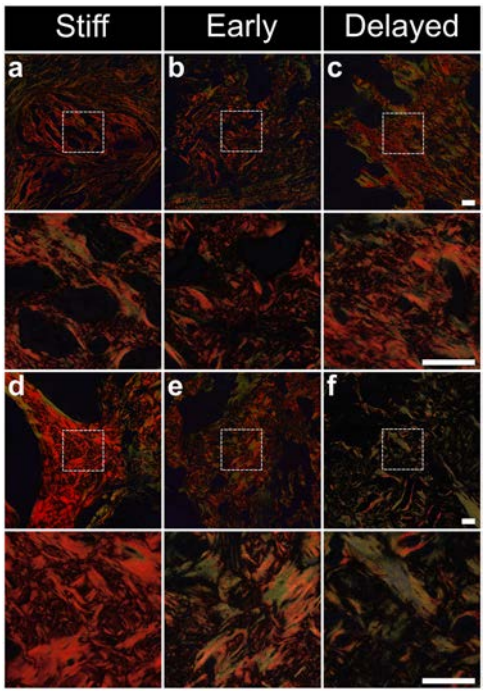

Extended Data Figure 6: Collagen organization. Photomicrographs of picrosirius red staining obtained using polarized light microscopy on sections at week 4 (**a-c**) and 12 (**d-f**). No differences between groups were apparent at week 4, and were characterized primarily by woven bone, but by week 12, both early and delayed loading groups exhibited reduced collagen fiber birefringence compared to stiff controls, indicative of prolonged new bone formation or delayed remodelling to lamellar bone (n = 1 per group at each time point, chosen by proximity to mean bone volume *in vivo* at 4 and 12 weeks). Under polarized light, large collagen fibers birefringe yellow and orange, while thinner fibers are green. Images are shown at 10x (top) and 40x (bottom) magnification of dotted boxes. Scale bars, 100 μm.

bioRxiv preprint doi: https://doi.org/10.1101/157362; this version posted June 29, 2017. The copyright holder for this preprint (which was not certified by peer review) is the author/funder, who has granted bioRxiv a license to display the preprint in perpetuity. It is made available under aCC-BY-NC-ND 4.0 International license.

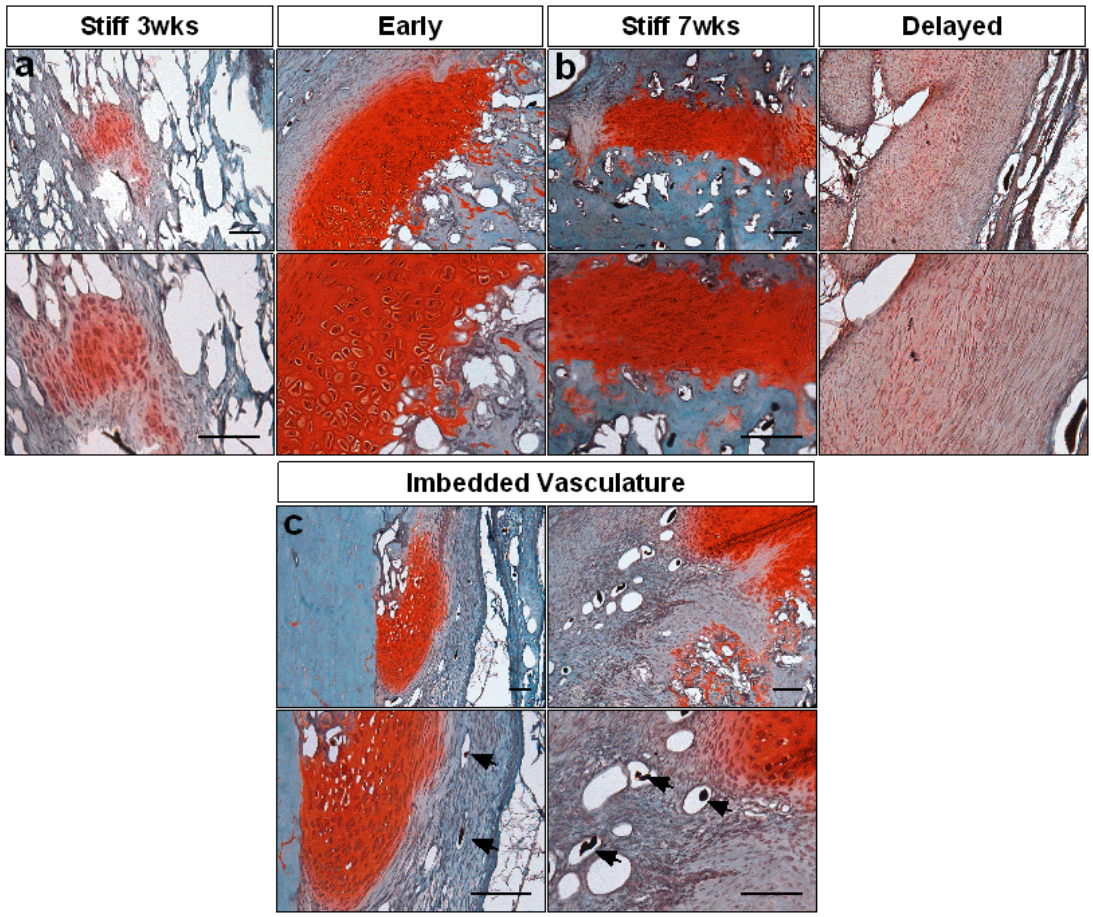

Extended Data Figure 7: Histology of contrast agent-perfused sections. Safranin-O/Fast green staining at 10x (top) and 20x (bottom) of sagittal histological sections of defects at **a,** 3 weeks with early loading and **b,** 7 weeks with delayed loading, shown alongside stiff contralateral controls at either time point (n = 3 per group at each time point, chosen by proximity to mean vessel volume at 3 and 7 weeks) displaying increased cartilage with early loading. **c,** Additional Safranin-O/Fast green sections at 10x (top) and 20x (bottom) of early (left) and stiff (right) illustrate invading vascular imbedded in bone matrix adjacent to cartilage, indicative of endochondral ossification. Patent vessels can be identified by residual perfuesed contrast agent (arrows). Scale bars, 100 µm.

bioRxiv preprint doi: https://doi.org/10.1101/157362; this version posted June 29, 2017. The copyright holder for this preprint (which was not certified by peer review) is the author/funder, who has granted bioRxiv a license to display the preprint in perpetuity. It is made available under aCC-BY-NC-ND 4.0 International license.

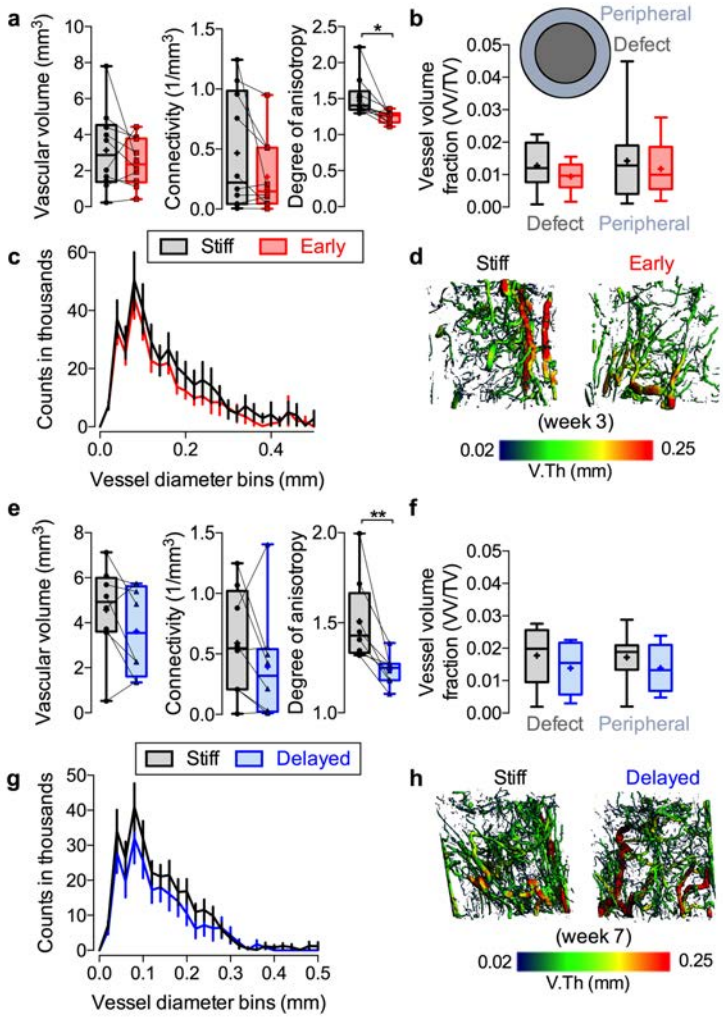

Extended Data Figure 8: Vasculature in defect periphery. Vessel volume, connectivity, and anisotropy of **a,** early loaded limbs (n = 10) compared to contralateral stiff controls in a 7mm region of interest that included vasculature from peripheral muscle, where no differences were seen in any morphometric parameter in either group apart from vessel anisotropy (*p<.05, **p<0.01, two-way paired student's t-test). Paired individual data points are superimposed on box plots displaying median as horizontal line, inter-quartile range as boxes, and min/max range as whiskers. Mean values are indicated by +. **b,** Region of interest analysis demonstrating no differences in vascular volume fraction in the 5mm diameter defect region compared to the 7mm-5mm peripheral region that included surrounding muscle (inset; two-way ANOVA with Tukey's *post-hoc* comparisons). Box plots display median as horizontal line, inter-quartile range as boxes, and min/max range as whiskers. Mean values are indicated by +. **c,** Histograms of vessel diameter bins indicating similar vessel thickness distribution between groups, and **d,** representative microCT angiography vessel thickness mapping. Vessel volume, connectivity, and anisotropy of **e,** delayed loaded limbs (n = 8) compared to contralateral stiff controls in the same 7mm region where again no differences were seen in any morphometric parameter in either group apart from vessel anisotropy (*p<.05, **p<0.01, two-way paired student's t-test). Data displayed as described previously. **f,** Region of interest analysis demonstrating no differences in vascular volume fraction in the defect region compared to the peripheral region (two-way ANOVA with Tukey's *post-hoc* comparisons). Data displayed as previously described. **g,** Histograms of vessel diameter bins and **h,** representative microCT angiography vessel thickness mapping. All representative images chosen by proximity to mean vessel volume.

bioRxiv preprint doi: https://doi.org/10.1101/157362; this version posted June 29, 2017. The copyright holder for this preprint (which was not certified by peer review) is the author/funder, who has granted bioRxiv a license to display the preprint in perpetuity. It is made available under aCC-BY-NC-ND 4.0 International license.

Extended Data Video 1: Fixation plate actuation and bone regeneration. Video animating plate configurations (top row) in which stiff plates minimize loading to the defect and compliant plates allow ambulatory load either immediately upon implantation (early) or after 4 weeks *in vivo* via surgical unlocking (delayed). Representative *in vivo* microCT reconstructions (bottom row) of regenerating defects at week 12, chosen by proximity to mean bone volume, demonstrate enhanced healing in the delayed group with complete bridging, while early and stiff groups failed to bridge by week 12, and stiff groups with devitalized constructs only achieved capping of bone ends.

bioRxiv preprint doi: https://doi.org/10.1101/157362; this version posted June 29, 2017. The copyright holder for this preprint (which was not certified by peer review) is the author/funder, who has granted bioRxiv a license to display the preprint in perpetuity. It is made available under aCC-BY-NC-ND 4.0 International license.

Materials and Methods

hMSC isolation and expansion. Human mesenchymal stem cells (hMSCs) were derived from the posterior iliac crest of a healthy male donor (41 years of age) using a protocol approved by the University Hospitals of Cleveland Institutional Review Board. Cells were isolated using a Percoll gradient (Sigma-Aldrich, St. Louis, MO) and cultured in low-glucose Dulbecco's modified Eagle's medium (DMEM-LG; Sigma-Aldrich, St. Louis, MO) containing 10% prescreened fetal bovine serum (FBS; Sigma-Aldrich) and 10 ng/ml fibroblast growth factor-2 (FGF-2, R&D Systems, Minneapolis, MN) as described previously.[10,31-32] Cells were verified to be negative for mycoplasma contamination during expansion, prior to *in vivo* implantation.

Gelatin microsphere synthesis and TGF-β1 loading. Gelatin microspheres were engineered and characterized as previously described.[10,32-33] Briefly, an aqueous solution of 11.1% (w/v) acidic gelatin type A (Sigma-Aldrich) was added drop-wise to 250 ml of preheated (45°C) olive oil (GiaRussa, Coitsville, OH) and stirred at 500 rpm for 10 min. The solution temperature was then lowered to 4°C with constant stirring. One hundred milliliters of chilled acetone were added to the solution after 30 min and again after 1 h. The solution was then stirred at 1000 rpm for 5 min. The resulting microspheres were collected by filtration, washed with acetone to remove residual olive oil, and dried overnight at room temperature. Microspheres were then crosslinked for 4 h with 1% (w/v) genipin (Wako USA, Richmond, VA), washed 3 times with diH_2O, and lyophilized. Hydrated GM gelatin microspheres were light blue in color and spherical in shape with an average diameter of 52.9±40.2 μm (N=150) and a crosslinking density of 25.5 ± 7.0% as determined by light micrograph image analysis (ImageJ software; National Institutes of Health, Bethesda, MD) and ninhydrine assay, respectively, according to protocols described previous.[33-34] Growth factor-loaded microspheres were prepared by soaking crosslinked, UV-sterilized gelatin microspheres in a 80 μg/ml solution of TGF-β1 (Peprotech, Rocky Hill, NJ) in phosphate buffered saline (PBS) for 2 h at 37°C. To ensure 100% growth factor binding, the volume of TGF-β1 solution used was less than the equilibrium swelling volume of gelatin microspheres. Unloaded microspheres without growth factor were hydrated similarly using only PBS. The release profile of TGF-β1 from crosslinked gelatin microspheres comprises an initial burst of ~60% by 20 h followed by complete release of all loaded growth factor in a linear fashion by 10 d.[32]

bioRxiv preprint doi: https://doi.org/10.1101/157362; this version posted June 29, 2017. The copyright holder for this preprint (which was not certified by peer review) is the author/funder, who has granted bioRxiv a license to display the preprint in perpetuity. It is made available under aCC-BY-NC-ND 4.0 International license.

Microsphere-incorporated hMSC sheet preparation. Expanded hMSCs ($2x10^6$ cells/sheet; passage 4) were thoroughly mixed with TGF-β1-loaded gelatin microspheres (400 ng/mg; 1.5 mg/sheet) in serum-free, chemically defined medium comprised of DMEM-HG (Sigma-Aldrich) with 10% ITS^+ Premix (Corning), 1 mM sodium pyruvate (HyClone), 100 μM non-essential amino acids (Lonza), 100 nM dexamethasone (MP Biomedicals, Solon, OH), and 0.05 mM L-ascorbic acid-2-phosphate (Wako) as described previously.[10] Five hundred microliter of the suspension were seeded onto the pre-wetted membrane of transwell inserts (3-μm pore size, 12-mm diameter; Corning) using large orifice tips and allowed to self-assemble for 2 days. After 24 h, the medium in the lower compartment was replaced with 1.5 ml of fresh chemically defined medium. Control sheets incorporated with unloaded gelatin microspheres were prepared and cultured in a similar fashion. After 48 h, hMSC sheets embedded with TGF-β1-loaded gelatin microspheres were used for implantation. Sheets designated for *in vitro* analysis were harvested and cut in half at the midline using a razor blade.

Quantitative reverse transcription-polymerase chain reaction (qRT-PCR) analysis. hMSC sheet halves (N=3/group) were homogenized in TRI Reagent (Sigma-Aldrich) for subsequent total RNA extraction and cDNA synthesis (PrimeScript™ 1st strand cDNA Synthesis Kit; Takara Bio Inc., Kusatsu, Shiga, Japan). One hundred nanograms of cDNA were amplified in duplicates in each 40-cycle reaction using a Mastercycler (Eppendorf, Hauppauge, NY) with annealing temperature set at 60ºC, SYBR® Premix Ex Taq™ II (Takara), and custom-designed qRT-PCR primers (Table I; Life Technologies, Grand Island, NY). Transcript levels were normalized to GAPDH and gene expression was calculated as fold change using the comparative C_T method.[35]

Gene		Sequence (5'-3')	Accession number
SOX9	Fwd	CACACAGCTCACTCGACCTTG	NM_000346.3
	Rev	TTCGGTTATTTTTAGGATCATCTCG	
ACAN	Fwd	TGCGGGTCAACAGTGCCTATC	NM_001135.3
	Rev	CACGATGCCTTTCACCACGAC	
COL2A1	Fwd	GGAAACTTTGCTGCCCAGATG	NM_001844.4
	Rev	TCACCAGGTTCACCAGGATTGC	
OSX	Fwd	TGGCTAGGTGGTGGGCAGGG	NM_001173467.2
	Rev	TGGGCAGCTGGGGGTTCAGT	

bioRxiv preprint doi: https://doi.org/10.1101/157362; this version posted June 29, 2017. The copyright holder for this preprint (which was not certified by peer review) is the author/funder, who has granted bioRxiv a license to display the preprint in perpetuity. It is made available under aCC-BY-NC-ND 4.0 International license.

TABLE I:

RUNX2	Fwd	ACAGAACCACAAGTGCGGTGCAA	NM_001015051.3
	Rev	TGGCTGGTAGTGACCTGCGGA	
ALP	Fwd	CCACGTCTTCACATTTGGTG	NM_000478.4
	Rev	GCAGTGAAGGGCTTCTTGTC	
COL1A1	Fwd	GATGGATTCCAGTTCGAGTATG	NM_000088.3
	Rev	GTTTGGGTTGCTTGTCTGTTTG	
GAPDH	Fwd	GGGGCTGGCATTGCCCTCAA	NM_002046.5
	Rev	GGCTGGTGGTCCAGGGGTCT	
YAP	Fwd	CAACTCCAACCAGCAGCAACA	NM_001130145
	Rev	GCAGCCTCTCCTTCTCCATCTG	
TAZ	Fwd	ACCCACCCACGATGACCCCA	NM_015472
	Rev	GCACCCTAACCCCAGGCCAC	
CTGF	Fwd	AGGAGTGGGTGTGTGACGA	NM_001901
	Rev	CCAGGCAGTTGGCTCTAATC	
CYR61	Fwd	GAGTGGGTCTGTGACGAGGAT	NM_001554
	Rev	GGTTGTATAGGATGCGAGGCT	

Oligonucleotide primer sequences for qRT-PCR.

Surgical procedure. Critical-sized (8-mm) bilateral segmental defects were created in the femora of twenty 14 week-old male Rowett nude (RNU) rats (Charles River Labs, Wilmington, MA) under isoflurane anesthesia, as previously described.[36] Briefly, anterolateral incisions were made over the length of each limb, and the vastus intermedius and vastus lateralis muscles were blunt-disected to expose the femur. Limbs were stabilized by custom internal fixation plates that allow controlled transfer of ambulatory loads *in vivo*[37] and secured to the femur by four bi-cortical miniature screws (J.I. Morris Co, Southbridge, MA). The experimental design featured three groups. Control limbs (stiff) were stabilized with fixation plates that limited load transfer (n=16). Early loading limbs were stabilized by axially compliant fixation plates that allowed load transfer immediately upon implantation (early, n=12). Delayed loading limbs were stabilized by the same compliant plates initially implanted in a locked configuration to prevent loading, but after four weeks the plates were surgically unlocked to enable load transfer (n=12). Fixation plate mechanical characterization is detailed in Extended Data Figure 2. Combination of treatment groups in each animal was chosen at random, but the surgeon was not blinded during the procedure due to fixation plate variation. During surgery, one animal was sacrificed under anesthesia, and three limbs were left untreated due to plate complications for a final sample number of n=13, 11, 11 for stiff, early, and delayed, respectively. In all three groups, each defect received three high-density cell sheets contained within an electrospun, perforated, poly-(ε-caprolactone) (PCL) nanofiber mesh tube for a total of $6x10^6$ cells and

bioRxiv preprint doi: https://doi.org/10.1101/157362; this version posted June 29, 2017. The copyright holder for this preprint (which was not certified by peer review) is the author/funder, who has granted bioRxiv a license to display the preprint in perpetuity. It is made available under aCC-BY-NC-ND 4.0 International license.

1.8 μg TGF-β1 per defect. Animals were given subcutaneous injections of 0.04 mg/kg buprenorphine every 8 h for the first 48 h postoperative (post-op) and 0.013 mg/kg every 8 h for the following 24 h. All procedures were reviewed and approved by the Institutional Animal Care and Use Committee (IACUC) at the University of Notre Dame (Protocol No. 14-05-1778).

Nanofiber mesh production. Nanofiber meshes were formed as described previously[16] by dissolving 12% (w/v) poly-(ε-caprolactone) (PCL; Sigma-Aldrich, St. Louis, MO) in 90/10 hexafluoro-2-propanol/dimethylformamide (HFP/DMF) (Sigma-Aldrich, St. Louis, MO). The solution was electrospun at a rate of 0.75 ml/h onto a static aluminum collector. 9 mm x 20 mm sheets were cut from the product, perforated with a 1 mm biopsy punch (VWR), and glued into tubes around a 4.5 mm mandrel with UV glue (Dymax, Torrington, CT). Meshes were sterilized by 100% ethanol evaporation and washed 3x with sterile phosphate buffered saline (PBS; Lonza) before implantation.

Fixation plate mechanical characterization. Characterization of the axial, torsional, and flexural plate stiffness was performed by screwing the plate onto two stainless steel 5/32" diameter rods through the tapped holes in the plate designed for bone screws. Axial tests were conducted in both the fixed-fixed and fixed-free configurations on the three plate configurations with a control rate of 0.02 mm/s to a displacement of 1.2 mm for the unlocked compliant and 0.005 mm/s to a displacement of 0.2 mm for stiff and locked compliant. Torsional tests were conducted in stiff, locked compliant, and unlocked compliant with a control rate of 0.1 deg/s to a displacement of 5 deg. Four-point bending tests were conducted using 5/32" square rods in the convex, concave, and side orientations on the three plate configurations with a control rate of 0.05 mm/s to a displacement of 2 mm for the unlocked compliant and 0.05 mm/s to a displacement of 1.5 mm for stiff and locked compliant. The stiffness under each loading condition was calculated as the slope of the linear region of the load-displacement curves.

In vivo X-ray and microCT. *In vivo* X-rays and microCT scans were performed at 4, 8, and 12 weeks to determine bridging and assess bone volume of the defect respectively. *In vivo* CT scans were performed on an Albira PET/SPECT/CT system (Bruker, Billerica, MA) at 45 kVp, 0.4 mA, with best resolution (125 μm voxel

bioRxiv preprint doi: https://doi.org/10.1101/157362; this version posted June 29, 2017. The copyright holder for this preprint (which was not certified by peer review) is the author/funder, who has granted bioRxiv a license to display the preprint in perpetuity. It is made available under aCC-BY-NC-ND 4.0 International license.

size). 45 slices were analyzed in the center of each defect with a global threshold of 400 to determine bone volume. X-rays were taken using an Xtreme scanner (Bruker, Billerica, MA) at 45 kVp, 0.4 mA, with 2 second exposure time. A binary bridging was score was assigned by two independent, blinded observers, and determined as mineralized tissue fully traversing the defect.

Ex vivo microCT. After 12 weeks the animals were euthanized by CO_2 asphyxiation and hind limbs (n=10, 8, 8 for stiff, early, and delayed respectively) were excised for high resolution microCT analysis using a Scanco µCT 80 system (Scanco Medical, Bassersdorf, Switzerland) at 70 kVp, 114 µA, at medium resolution (20 µm voxel size). 302 slices in the center of each defect were analyzed with a threshold corresponding to 488 mg HA/ccm, gauss filter width of 0.8, and filter support of 1.0. Two regions of interest (ROI) were analyzed; a 5 mm diameter circle centered on the medullary canal termed "defect", and a "total" region in which any remaining bone outside the 5 mm defect was additively contoured. A third region, "ectopic", was calculated by subtracting defect from total ROI. Bone volume, mineral density, bone volume fraction, polar moment of inertia (pMOI), and the morphometric parameters connectivity density, trabecular thickness, trabecular spacing, and trabecular number were calculated using a built-in algorithm that fits a maximal sphere in either the pore or trabecular strut at each voxel in the 3D space (Scanco evaluation script "V6"). Trabecular morphometry of three age-matched femoral heads were analyzed in the same manner for comparison. Proximal and distal total bone volume were calculated by halving the slice number in each sample and separately segmenting each half for comparison. All postmortem representative images were chosen based on average value for each illustrated parameter.

Biomechanical testing. Femora (n=8, 7, 7 for stiff, early, and delayed respectively) excised at 12 weeks were biomechanically tested in torsion to failure. Limbs were cleaned of soft tissue and the fixation plate was carefully removed. Bone ends were potted in Wood's metal (Alfa Aesar), mounted on a Bose ElectroForce biaxial load frame system (ELF 330, Bose EnduraTEC) and tested to failure at a rate of 3 degrees per second. For each sample maximum torque at failure was recorded and torsional stiffness was determined as the slope of a 5 degree linear region in the torque-rotation curve. Samples were compared to 7 age matched, un-operated femurs.

bioRxiv preprint doi: https://doi.org/10.1101/157362; this version posted June 29, 2017. The copyright holder for this preprint (which was not certified by peer review) is the author/funder, who has granted bioRxiv a license to display the preprint in perpetuity. It is made available under aCC-BY-NC-ND 4.0 International license.

Histological analysis. hMSC sheet halves (n=3/group) were fixed in 10% neutral buffered formalin (NBF) for 24 h at 4ºC before switching to 70% ethanol. One representative femur per group was taken for histology at weeks 4 and 12 post-surgery, chosen based on microCT-calculated average bone volumes. Samples were fixed in 10% NBF for 72 h at 4ºC and then transferred to 0.25 Methylenediaminetetraacetic acid (EDTA) pH 7.4 for 14 d at 4ºC under mild agitation on a rocker plate, with changes of the decalcification solution every 3-4 days. Following paraffin processing, 5-µm mid-saggital sections were cut using a microtome (Leica Microsystems Inc., Buffalo Grove, IL, USA) and stained with hematoxylin & eosin (H&E), Safranin-O/Fast-green (Saf-O), and picrosirius red (PSR; Polysciences, Inc., Warrington, PA). Light microscopy images, employing linearly polarized light for PSR-stained sections, were captured using an Olympus BX61VS microscope (Olympus, Center Valley, PA, USA) with a Pike F-505 camera (Allied Vision Technologies, Stadtroda, Germany).

Immunohistochemistry. Formalin fixed, paraffin embedded hMSC sheets and decalcified femurs were deparaffinized and rehydrated in successive incubations in xylene, ethanol, and diH_2O. Heat induced antigen retrieval was performed for 8 minutes at 90°C in a Tris-EDTA antigen retrieval buffer; 10 mM Tris-base, 1 mM EDTA, 0.05% tween-20, pH 9.0. Endogenous peroxidase activity was quenched in .3% hydrogen peroxide in methanol. Non-specific binding was blocked using either serum-free protein block (DAKO; Santa Clara, CA, USA), for rabbit primary antibodies, or 2.5% horse serum from the RTU Vectastain Kit (Vector; Burlingame, CA, USA), for mouse primary antibodies. All primary antibodies were incubated overnight at 4°C. Rabbit primary antibodies were detected using Signal Stain Boost IHC Detection Reagent (Cell Signaling; Danvers, MA, USA) and mouse primary antibodies were detected using biotinylated universal secondary antibodies followed by incubation with streptavidin conjugated peroxidase from the RTU Vectastain Kit. Colorimetric antibody detection was performed using ImmPACT DAB peroxidase substrate kit (Vector) and counterstained with hematoxylin. Rabbit primary antibodies were yes-associated protein (YAP; D8H1X; Cell Signaling), transcriptional coactivator with PDZ-binding motif (TAZ; V386; Cell Signaling), and rabbit isotype control IgG (IgG; DA1E; Cell Signaling). Mouse primaries were connective tissue growth factor (CTGF; ab6992; abcam; Cambridge, MA, USA), cysteine rich angiogenic inducer (CYR61; ab80112; abcam), and human nuclear antigen (HUNU; MAB1281; EMD Millipore; Darmstadt, Germany).

bioRxiv preprint doi: https://doi.org/10.1101/157362; this version posted June 29, 2017. The copyright holder for this preprint (which was not certified by peer review) is the author/funder, who has granted bioRxiv a license to display the preprint in perpetuity. It is made available under aCC-BY-NC-ND 4.0 International license.

Devitalized cell delivery. hMSC sheets (identical to previously described, using the same cells and growth factor presentation) were devitalized by 3 freeze/thaw cycles. Three devitalized sheets were placed into each electrospun, perforated, nano-mesh cylinder and placed in a critically-sized segmental defects (8mm) under stiff fixation (n=5). Limbs were assessed by *in vivo* microCT at 4, 8, and 12 weeks, and *ex vivo* microCT at 12 weeks for comparison with live cell delivery under stiff fixation.

MicroCT angiography. Critically sized (8mm) segmental defect surgery was repeated in twenty 14 week-old male Rowett nude (RNU) rats (Charles River Labs, Wilmington, MA) under isoflurane anesthesia. In each rat a loaded limb, either early (n=10) or delayed (n=8) was paired with a contralateral control limb, stabilized by a stiff fixation plate that limited load transfer (stiff, n=18 total). Two animals were lost in the delayed group due to plate complications. Contrast enhanced microCT angiography was performed at week 3 in the early loading group and week 7 in the delayed group. Radiopaque contrast agent-enhanced microCT angiography was performed using a protocol modified from that described previuosly[24,38] Briefly, the vasculature was perfused through the ascending aorta with sequential solutions of heparin, saline, 10% formalin, and lead chromate-based radiopaque contrast agent (Microfil MV-122, Flow Tech). After perfusion, limbs were excised and scanned via microCT (as described above) with both bone and contrast agent intact. Limbs were then decalcified with formic acid for 2 weeks, scans were repeated, and subtraction was used to distinguish between bone and vessel parameters in a 5 mm diameter defect region of interest (ROI) and 7 mm diameter total ROI. Three representative samples from each group, chosen based on average microCT-computed vessel volume, were processed for histology.

Cationic cartilage contrast-enhanced microCT. The cationic iodinated contrast agent, CA^{4+}, was prepared as described previuosly,[49] at a concentration of 24 mg I/mL, pH 7.4, and osmolality of 400 mOsm/kg. The paired early/stiff and delayed/stiff limbs, previously analysed by microCT angiography, were scanned before incubation and after 4 and 10 days of incubation. Day 10 scans were used for quantitative analysis. Limbs were incubated in 1.6 mL of CA^{4+}) solution at room temperature. For the first hour of incubation and the last hour before each scan, sample tubes were incubated in a benchtop ultrasonic cleaner (model 97043-960, VWR) using a protocol modified from that previously described[50]. One stiff and one delayed limb (not paired) were lost from the

bioRxiv preprint doi: https://doi.org/10.1101/157362; this version posted June 29, 2017. The copyright holder for this preprint (which was not certified by peer review) is the author/funder, who has granted bioRxiv a license to display the preprint in perpetuity. It is made available under aCC-BY-NC-ND 4.0 International license.

delayed/stiff group due to tissue preparation error. MicroCT analysis was performed using a Scanco µCT 80 system (Scanco Medical, Bassersdorf, Switzerland) at 70 kVp, 114 µA, at a resolution of 15.6 µm/voxel. A region in the center of each defect was analyzed corresponding to the smallest defect in each group, 410 slices in early/stiff and 455 slices in stiff/delayed. Subtraction was used to distinguish between cartilage and vessel parameters in a 5 mm diameter "annulus" region of interest (ROI) and 1.5 mm diameter "core" ROI, centered on the medullary canal as determined by surgical screw placement in each sample. Registration of scans before and after incubation was performed using Analyze 10.0.

Statistics. Bridging rates were assessed by chi-square test for trend (*$p<0.05$) and are presented as percent of samples bridged in each group; comparisons between groups were assessed with individual chi-squared tests and Bonferroni correction for multiple comparisons. Comparisons between groups were assessed by one- or two-way analysis of variance (ANOVA) with Tukey's multiple comparison tests (*$p<0.05$), as appropriate. The relationship between pMOI and mechanical characteristics was determined via linear regression. Raw data are displayed with mean ± s.d or as box plots showing 25th and 75th percentiles, with whiskers at minimum and maximum values. Where necessary and appropriate, data were log transformed to ensure normality and homoscedasticity prior to ANOVA. Normality of dependent variables and residuals were verified by D'Agostino-Pearson omnibus and Brown-Forsythe tests, respectively. In the devitalized cell experiment, surgical implantation and evaluation for this group was performed at a separate time from the live cell analysis and was therefore not included in quantitative statistical comparisons, though the presence of this group was accounted for in the ANOVA and post-hoc multiple comparisons shown in Figure 2c.

Differences in angiography between loaded samples and stiff samples were assessed by paired two-way student's t-tests (*$p<0.05$), accounting for animal variability perfusion efficacy. Statistical comparisons were performed using GraphPad Prism (La Jolla, CA, USA). The sample sizes for microCT, mechanical testing, and contrast enhanced angiography analyses were determined with G*Power software[39] based on a power analysis using population standard deviations and estimated effect sizes from our prior studies.[4,17,40] The power analysis assumed a two-tailed alpha of 0.05, power of 0.8, and effect sizes of ranging from 0.1 to 0.3. A minimum sample number of n = 6 per group was computed, with an ideal sample number of n = 12 for all non-destructive and

bioRxiv preprint doi: https://doi.org/10.1101/157362; this version posted June 29, 2017. The copyright holder for this preprint (which was not certified by peer review) is the author/funder, who has granted bioRxiv a license to display the preprint in perpetuity. It is made available under aCC-BY-NC-ND 4.0 International license.

destructive analyses per time point. An n = 10 was selected for all non-destructive and destructive analyses per time point, accommodating a 5-10% complication rate consistent with our prior studies.

References

4. Boerckel JD, Uhrig B a, Willett NJ, Huebsch N, Guldberg RE. Mechanical regulation of vascular growth and tissue regeneration in vivo. Proc Natl Acad Sci U S A. 2011 Aug 29;108(37):E674-80. PMID: 21876139

10. Solorio LD, Vieregge EL, Dhami CD, Dang PN, Alsberg E. Engineered cartilage via self-assembled hMSC sheets with incorporated biodegradable gelatin microspheres releasing transforming growth factor-β1. J Control Release. 2012;158(2):224–232.

16. Kolambkar YM, Dupont KM, Boerckel JD, Huebsch N, Mooney DJ, Hutmacher DW, Guldberg RE. An alginate-based hybrid system for growth factor delivery in the functional repair of large bone defects. Biomaterials. Elsevier Ltd; 2011 Jan;32(1):65–74. PMID: 20864165

17. Dupont KM, Sharma K, Stevens HY, Boerckel JD, García AJ, Guldberg RE. Human stem cell delivery for treatment of large segmental bone defects. Proc Natl Acad Sci U S A. 2010 Feb 23;107(8):3305–10. PMID: 20133731

24. Boerckel JD, Mason DE, McDermott AM, Alsberg E. Microcomputed tomography: approaches and applications in bioengineering. Stem Cell Res Ther. 2014 Jan;5(6):144. PMID: 25689288

31. Solorio LD, Dhami CD, Dang PN, Vieregge EL, Alsberg E. Spatiotemporal regulation of chondrogenic differentiation with controlled delivery of transforming growth factor-beta1 from gelatin microspheres in mesenchymal stem cell aggregates. Stem Cells Transl Med. 2012 Aug;1(8):632–639.

32. Dang PN, Dwivedi N, Phillips LM, Yu X, Herberg S, Bowerman C, Solorio LD, Murphy WL, Alsberg E. Controlled dual growth factor delivery from microparticles incorporated within human bone marrow-derived mesenchymal stem cell aggregates for enhanced bone tissue engineering via endochondral ossification. Stem Cells Transl Med. AlphaMed Press; 2016;5(2):206–217.

bioRxiv preprint doi: https://doi.org/10.1101/157362; this version posted June 29, 2017. The copyright holder for this preprint (which was not certified by peer review) is the author/funder, who has granted bioRxiv a license to display the preprint in perpetuity. It is made available under aCC-BY-NC-ND 4.0 International license.

33. Dang PN, Solorio LD, Alsberg E. Driving cartilage formation in high-density human adipose-derived stem cell aggregate and sheet constructs without exogenous growth factor delivery. Tissue Eng Part A. Mary Ann Liebert, Inc. 140 Huguenot Street, 3rd Floor New Rochelle, NY 10801 USA; 2014;20(23–24):3163–3175.

34. Solorio L, Zwolinski C, Lund AW, Farrell MJ, Stegemann JP. Gelatin microspheres crosslinked with genipin for local delivery of growth factors. J Tissue Eng Regen Med. Wiley Online Library; 2010;4(7):514–523.

35. Schmittgen TD, Livak KJ. Analyzing real-time PCR data by the comparative CT method. Nat Protoc. Nature Publishing Group; 2008;3(6):1101–1108.

36. Oest ME, Dupont KM, Kong H, Mooney DJ, Guldberg RE. Quantitative Assessment of Scaffold and Growth Factor-Mediated Repair of Critically Sized Bone Defects. J Orthop Res. 2007;(July):941–950.

37. Boerckel JD, Dupont KM, Kolambkar YM, Lin ASP, Guldberg RE. In vivo model for evaluating the effects of mechanical stimulation on tissue-engineered bone repair. J Biomech Eng. 2009;131(8):84502. PMID: 19604025

38. Duvall CL, Taylor WR, Weiss D, Guldberg RE. Quantitative microcomputed tomography analysis of. Am J Physiol Hear Circ Physiol. 2004;287:H302–H310.

39. Faul F, Erdfelder E, Buchner A, Lang A-G. Statistical power analyses using G* Power 3.1: Tests for correlation and regression analyses. Behav Res Methods. Springer; 2009;41(4):1149–1160.

40. Uhrig BA, Boerckel JD, Willett NJ, Li M-TA, Huebsch N, Guldberg RE. Recovery from hind limb ischemia enhances rhBMP-2-mediated segmental bone defect repair in a rat composite injury model. Bone. 2013;55(2):410–417.